Report on Activities Related to MTSL RADFET Dosimeters Development and Supply During the 2000/2001 Programme

Confidentiality Status: **Commercial-in-confidence**

Prepared for: **Ali Mohammadzadeh, ESA-ESTEC**

Prepared by: **Aleksandar Jaksic**

Date: **January 28, 2002**

Devices & Systems for Dosimetry, Transducers Group
National Microelectronics Research Centre (NMRC)
University College Cork, Lee Maltings, Prospect Row, Cork, Ireland
http://www.nmrc.ie/projects/radfets/index.html
Tel.: +353 21 490 4262
Fax: +353 21 427 0271
Email: ajaksic@nmrc.ie

Contents:

Introduction

This document contains description of the most relevant activities and results related to 2000/2001 MTSL RADFET Dosimeters Development and Supply Programme. This one-year programme was carried out under the Contract No. 10582/93/NL/PB, Work Order No. 06, Call-off Order No. 21.

The report follows a structure of work-packages and corresponding deliverables from 2000/2001 programme, as given in the NMRC WP03 proposal dated 30/06/2000. Besides the main body of the report, the following Appendices constitute an important part of the report, where additional relevant information is given in more detail:

- Appendix 1: RADECS 2001 final paper,
- Appendix 2: MIEL 2002 final paper,
- Appendix 3: Report on PSI Irradiation Campaign in June 2001.

Description of Activities and Results by Work-Packages

Work-package 1: Supply of RADFETs

Table 1 gives the list of RADFETs delivered to ESTEC during the programme.

Table 1: RADFETs delivered to ESTEC during 2000/2001 programme.

Description	Lot No.	Qty.
400nm Unimpl, ESAPMOS2, bare die	P172-W10	10
400nm Impl, ESAPMOS2, bare die	P210-W7	5
400nm Impl, ESAPMOS2, bare die	P210-W9	5
400nm Impl, ESAPMOS4, bare die	P1152-W2	20
400nm Impl, ESAPMOS4, 14-pin DIL	P1152-W2	46[1]
400nm Impl, ESAPMOS4, 8-pin DIL	P1152-W2	45

The delivery of packaged devices included documentation designed to give some technical specifications and help end-user to understand the RADFET operation in practical applications. These documents will serve as a basis for development of a more comprehensive set of the RADFET technical documentation.

There were no irradiation campaigns at ESTEC during realisation of the programme, the main reason being delays with the RADFET Reader Board system (see Work-package 2 below). However, in December 2000, irradiation experiments were performed at the Institute of Nuclear Sciences “Vinca”, Belgrade, Yugoslavia. Several RADFET types, mostly of ESAPMOS2 design, but also, for the first time, of ESAPMOS4 design (400nm Impl devices), were irradiated by a certified Co-60 source. Results related to ESAPMOS2 RADFETs are given in Appendix 1.

Table 2 summarises irradiation conditions for experimental ESAPMOS4 samples. The total irradiation dose was 5 krad, and the those rate 1.3 rad/s. The ESAPMOS4 RADFET chip contains four RADFETs, as follows[2]:

- RADFET 1: 300/50 RADFET with all terminals (Bulk, Source, Drain and Gate) accessible,
- RADFET 2: 690/15 RADFET with all terminals accessible,
- RADFET 3: 300/50 RADFET with Bulk and Source, as well as Drain and Gate tied together,
- RADFET 4: 690/15 RADFET with Bulk and Source, as well as Drain and Gate tied together.

During irradiation, the Bulk, Source and Drain terminals were grounded, while the Gate was either grounded or biased (irradiation bias $V_{irr} \equiv V_{GS}$). Hence, because of their internal configuration RADFETs 3 and 4 were always irradiated unbiased, even in the cases when RADFETs 1 and 2 from the same chips had non-zero V_{irr}.

The configuration that was used for threshold voltage (V_T) measurements in a remote mode (between subsequent radiation exposures) is a standard Reader Circuit (RC) configuration in Figure 1.

---

[1] 40 to ESTEC plus 6 to Beagle 2 team in the UK.
[2] The ESAPMOS4 RADFET chip layout is described in the document “ESAPMOS4 Chip Description”, supplied to ESTEC in 1999.

Table 2: Experimental ESAPMOS4 400nm Impl samples with irradiation bias (V_{irr}). The given V_{irr} values are valid for RADFETs 1 and 2 on the chip; as discussed above, V_{irr}=0V for RADFETs 3 and 4 in all cases.

Chip Label	Virr [V]
E38	-5
E39	-5
E40	0
E41	0
E42	+5
E43	+5

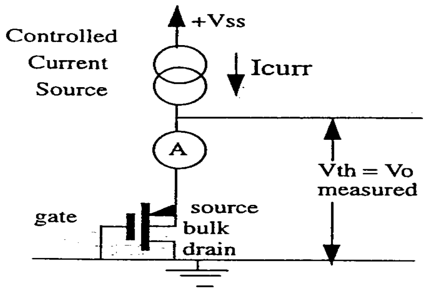

Figure 1: The Reader Circuit (RC) measurement configuration used for V_T measurements; Icurr = 10µA.

Main experimental results and conclusions are summarised below; more details are given in Appendix 2.

Table 3 shows the results of irradiation of ESAPMOS4 400nm Implanted RADFETs.

Table 3: Threshold voltage shifts ΔV_T[V] of the ESAPMOS4 400nm Implanted RADFETs during irradiation. Exx denotes the RADFET chip, V_{irr} is given in brackets.

RADFET 1 (300/50)

Dose (rad)	E38 (-5V)	E39 (-5V)	E40 (0V)	E41 (0V)	E43 (+5V)	E42 (+5V)
100	0.0280	0.0297	0.0816	0.0821	0.1549	0.1562
1000	0.2629	0.2698	0.7309	0.7290	1.4191	1.4631
5000	1.1042	1.1331	2.4809	2.4849	6.0993	6.3311

RADFET 3 (300/50)

Dose (rad)	E38 (0V)	E39 (0V)	E40 (0V)	E41 (0V)	E43 (0V)	E42 (0V)
100	0.0826	0.0835	0.0808	0.0825	0.0792	0.0804
1000	0.7363	0.7443	0.7141	0.7211	0.6847	0.7166
5000	2.4947	2.5188	2.4272	2.4522	2.3155	2.4382

RADFET 2 (690/15)

Dose (rad)	E38 (-5V)	E39 (-5V)	E40 (0V)	E41 (0V)	E43 (+5V)	E42 (+5V)
100	0.0233	0.0295	0.0768	0.0776	0.1521	0.1529
1000	0.2581	0.2656	0.7181	0.6894	1.4003	1.4365
5000	1.0743	1.1039	2.3529	2.3781	6.0802	6.2872

RADFET 4 (690/15)

Dose (rad)	E38 (0V)	E39 (0V)	E40 (0V)	E41 (0V)	E43 (0V)	E42 (0V)
100	0.0744	0.0772	0.0713	0.0759	0.0740	0.0746
1000	0.7114	0.7285	0.7043	0.7042	0.6928	0.7076
5000	2.3934	2.4456	2.3627	2.3752	2.2983	2.3845

Figure 2 plots the threshold voltage shifts (ΔV_T) from Table 3 for the typical 300/50 RADFET samples, irradiated with negative, zero and positive gate bias .

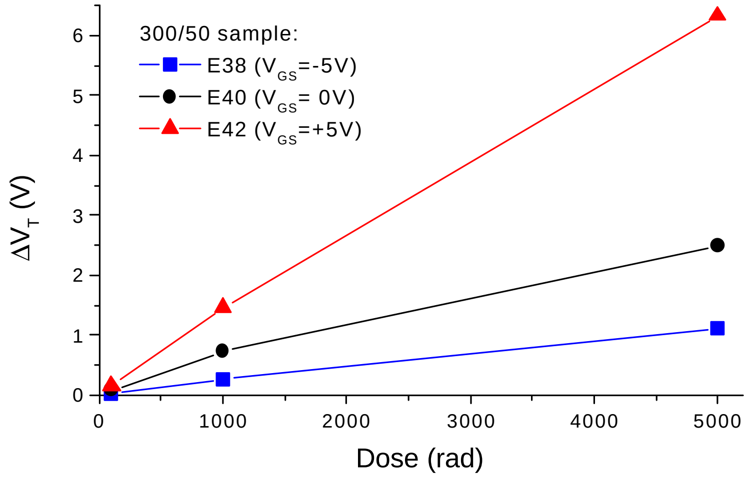

Figure 2: Threshold voltage shifts for the typical 300/50 samples from Table 3 irradiated with negative, zero and positive bias.

Table 4 summarises the mean sensitivities at different irradiation doses for 300/50 RADFETs. The sensitivity of the 690/15 RADFET closely follows that of the 300/50 device but is some 2-3% lower.

Table 4: Radiation sensitivity figures ([mV/cGy], 300/50 RADFET, RC configuration).

Dose (Gy)\V_{irr}	V_{irr}=-5V	V_{irr}=0V	V_{irr}=+5V
1	0.28	0.82	1.56
10	0.26	0.72	1.46
50	0.22	0.50	1.27

The sensitivity values in Table 4 are in good agreement with the values previously obtained for the ESAPMOS2 400nm Implanted RADFETs irradiated at ESTEC. This is the first indication that the change in the single RADFET chip design from ESAPMOS2 to ESAPMOS4 hasn't affected sensitivity of the 300/50 device. Unfortunately, small number of points in graphs in Figure 2 prevents fitting of the ΔV_T dependence on dose and comparison with the previously fitted power-law calibration curves. It is interesting to note that the sensitivity of the RADFETs irradiated with negative bias is lower than that of the RADFETs irradiated with zero bias. This is not always the case with RADFETs of other vendors[3]. The fact of lower sensitivity with negative gate bias is of importance for further BIOPAN Board characterisation, as the RADFET mounted on BIOPAN Board is biased with non-constant negative bias. Expectedly, the sensitivity of devices irradiated with positive bias is the highest.

The variations in radiation response of different experimental samples are small, and are typically within several percents for both 300/50 and 690/15 RADFETs. This is a very good result, having in mind the experimental uncertainties (e.g. homogeneity of the radiation field, distance of the samples from the radiation source, etc.).

<u>Work-package 2:</u> Energetic Particle Response

The prerequisite for the work on this work-package (as well as on Work-package 1) was design of the hardware and software for the so-called RADFET Reader Board (RRB) system. Admittedly, the complexity of the task was underestimated in the proposal for the 2000/2001 programme. Several different versions of the RRB were needed to get the necessary experience, realise and solve all the practical design problems. This finally resulted in the RRB hardware and software designs that provide many features and, in addition, are flexible, expandable, and user-friendly. It is expected that the introduction of the RRB system will lead to major improvements in RADFET characterisation work.

[3] See, for example, G. Ristic, S. Golubovic, M. Pejovic, "Sensitivity and fading of PMOS dosimeters with thick gate oxide", *Sensors and Actuators A*, vol. 51, pp. 153-158, 1996.

The complete RRB system is shown in Figure 3.

Figure 3: The complete RADFET Reader Board (RRB) system comprises (from left to right): a PC running a dedicated LabView program; Data Acquisition Card (DAC); RADFET Reader Control Board (RRCB) – down, and RADFET Socket Board (RSB) – up. The PC and DAC are outside the radiation room, RRCB is inside the room but shielded against radiation, and RSB with the RADFETs mounted on it is exposed to radiation.

The system consists of the following components:

- Personal Computer (PC)

  The only requirement for the PC is the existence of the RS-232 port, which is generally the case for all modern PCs. The NMRC will use a dedicated laptop PC in order to provide full portability of the RRB system.

- Data Acquisition Card (DAC)

  The type of the DAC is National Instruments Daq-Pad 1200. The DAC is connected to the PC via RS-232 bus and controlled by the National Instruments LabView 6.i program.

- RADFET Reader Control Board (RRCB)

  The RRCB (Figure 4) is custom designed PCB that enables biasing of the RADFET chips and read-out of the RADFET output voltage and temperature during irradiation. The RRCB is connected to and controlled by DAC. The connection is provided via the long parallel cable. The board is also connected to a ±20V standard laboratory power supply. Two identical RRCBs were manufactured.

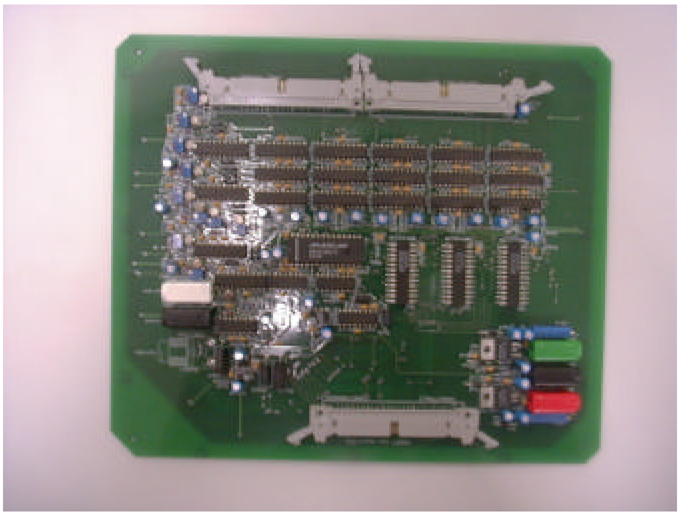

Figure 4: The RADFET Reader Control Board (RRCB). The 50-way connector at the bottom provides connection with DAC and two 50-way connectors at the top provide connection with RSB.

- RADFET Socket Board (RSB)

  The RSB (Figure 5) is the custom designed PCB with the RADFET chip sockets and temperature sensors. The RADFETs that are to be irradiated are placed in the sockets. The RSB is the only component of the RRB system that is not shielded against radiation during the system operation. The RSB is connected to RRCB via two 50-way connectors. Wires going from RRCB to RSB are flexible and should be rather short (up to 1m) in order to minimise the noise in the analogue part of the system but still enable shielding of the RRCB. There are two variants of the RSB: for ESAPMOS2 and ESAPMOS4 RADFETs. The total of four RSBs were manufactured, two each for ESAPMOS2 and ESAPMOS4 RADFET chips.

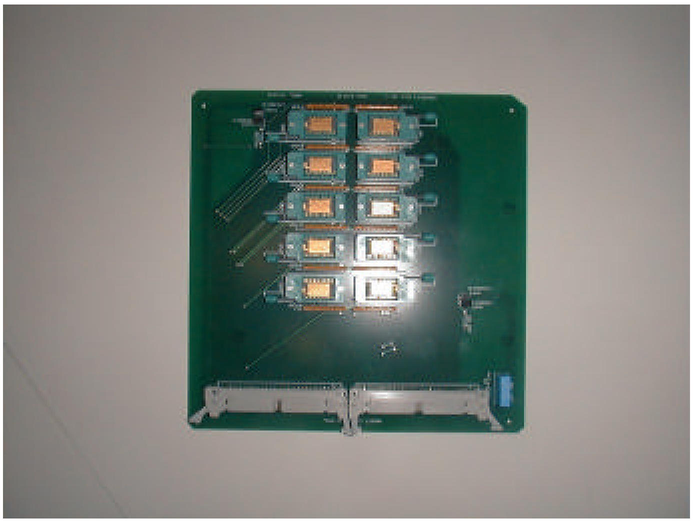

Figure 5: The RADFET Socket Board (RSB). The two 50-way connectors at the bottom provide connection with RRCB. The 10 RADFET sockets have RADFET chips mounted on them. The size of the area with RADFET chips is 10cm x 5cm. There are two temperature sensors: top left and down right from the RADFET chip area.

The main features of the RRB system include:

- The system can accommodate maximum 10 RADFET chips, i.e. the total of 40 individual RADFETs (ESAPMOS4 design) or 20 RADFETs (ESAPMOS2 design). Each individual chip and each RADFET on chip can be accessed (monitoring enabled or disabled).
- There is a choice of three RADFET biasing configurations (RADFET is in “irradiation” mode):

  (1) Zero gate bias (all RADFET terminals grounded),

  (2) Positive constant gate bias (RADFET Bulk, Source and Gate grounded, positive V_{irr} applied to the Gate),

  (3) Continuously applied constant current (as in Figure 1; this configuration is equivalent to the negative non-constant bias applied to the Gate during irradiation).
- There is a choice of three RADFET read-out configurations (RADFET is in “measurement” mode). These configurations are related to the mode of the read-out current, as follows:

  (1) Constant current from the internal RRCB source that is computer-controlled and adjusted to the specified nominal value (typically 10μA). The capability of adjusting the current is important, as the current from the standard source is not constant, but changes to some extent with the RADFET output voltage (see discussion within the Work-package 3 below).

  (2) Constant current from the internal RRCB source that can be manually adjusted using the variable setting resistor.

  (3) Constant current from the external high quality current source. In this case there is no need for current adjustment.
- The system is user-friendly, completely automated, and provides lot of useful experimental data that are stored in the computer. At the beginning, the user specifies individual RADFETs to be measured, irradiation and read-out configurations, desired times (absorbed doses) at which read-out is to be done and other pertinent details. After completion of the initial, pre-irradiation measurements (these measurements provide reference values), the execution of the program starts simultaneously with

switching on the radiation field. The RRB system then measures important experimental parameters for each specified individual RADFET at the specified times (doses), displays relevant information and stores the data in the computer. The stored data include time (dose), RADFET threshold voltage, threshold voltage shift, read-out current, temperature, sensitivity, etc.

Despite the fact that the RRB system was not ready at that time, the irradiation campaign at PSI was carried out in June 2001. Detailed report on PSI irradiation campaign is given in Appendix 3.

<u>Work-package 3:</u> BIOPAN support

Following the requirements of ESTEC, the previous version of the BIOPAN board was re-designed. The changes in the board design were aimed to simplify the board and eliminate possible sources of error during operation. The new board is populated with commercial (non-radiation-hardened components). Initial experiments at ESTEC with previous version of the board have shown rather stable performance of the non-radiation-active components in the irradiation field. Thus, it was concluded that the characterisation of the RADFET response in BIOPAN configuration and temperature stability are more important issues and re-design was made in line with this approach.

Figure 6 shows electrical schematics of the new version of the BIOPAN board. In fact, three versions of the board were designed, differing only in the operational amplifier used and related capacitors and/or resistors. The intention was to test three operational amplifiers with different characteristics and choose the best one for the final version of the board.

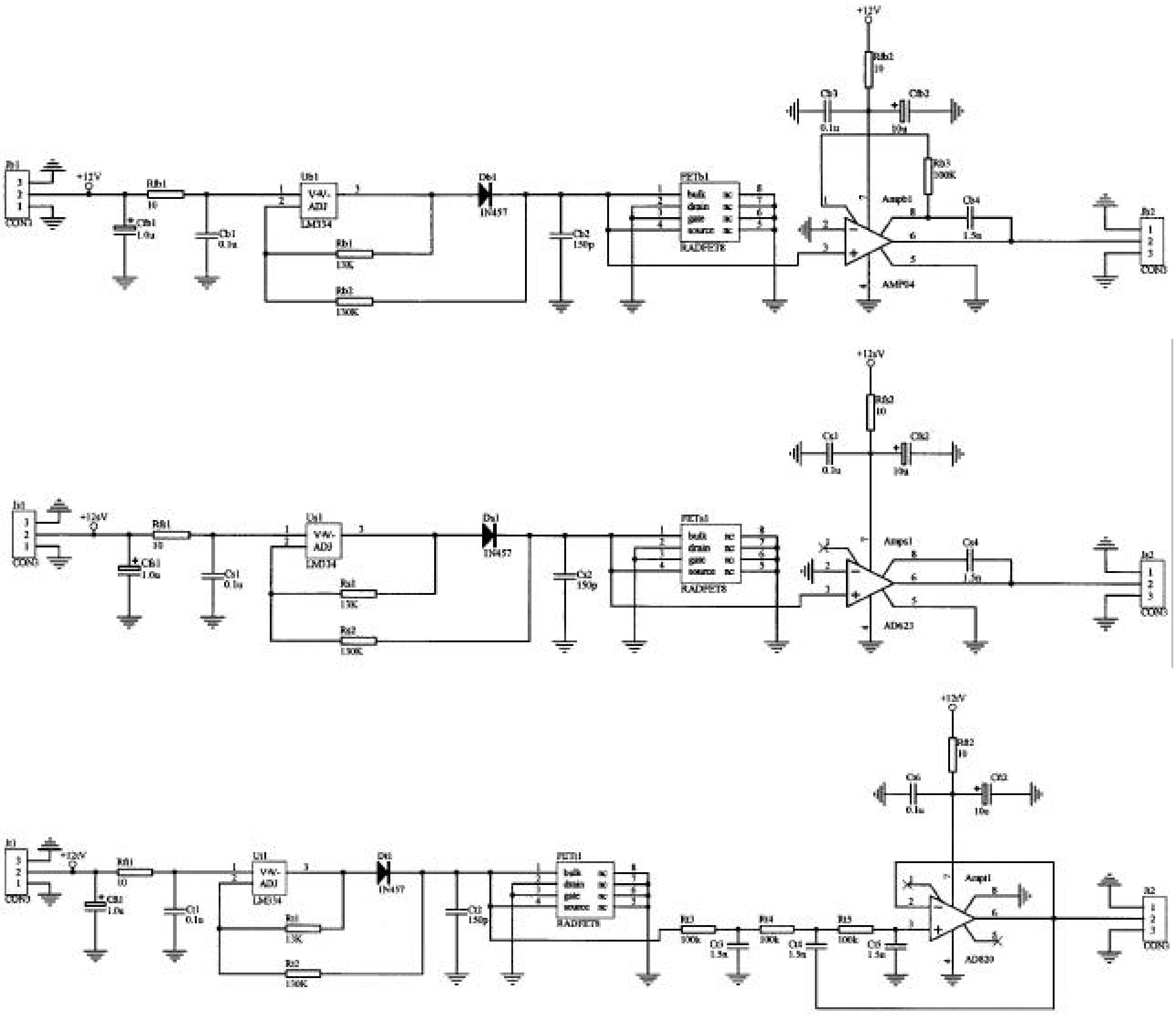

Figure 6: Electrical schematics of three versions of the re-designed BIOPAN board. The three versions differ in the type of operational amplifier used: Version 1 (top) – AMP04, Version 2 (middle) – AD623, and Version 3 (bottom) – AD820.

The three board versions in Figure 6 are:

- Version 1, using Opamp1 (AMP04)
- Version 2, using Opamp2 (AD623)
- Version 3, using Opamp3 (AD820)

Table 5 gives the list of components used in the new board design.

Table 5: The list of components used in the three versions of the re-designed BIOPAN board. The three board versions differ only in the type of the operational amplifier used and related resistors/capacitors.

Version 1 (Figure 6 - top)

Description	Designator	FootPrint	PartType
Three Terminal Adjustable Current Source	Ub1	TO92B	LM334
Diode	Db1	D_1N457	1N457
Resistor	Rb2	AXIAL - RC55(7.2X2.5)	130K
Resistor	Rb1	AXIAL - RC55(7.2X2.5)	13K
Capacitor	Cb1	CAPACITOR-S100	0.1u
Electrolytic Capacitor	Cfb2	ECAP-5X2	10u
Capacitor	Cb3	CAPACITOR-S100	0.1u
Resistor	Rfb2	AXIAL - MF12(4.2X2.0)	10
RADFET8 (RADFET in 8-pin DIP package)	FETb1	DIP 8	RADFET8
Resistor	Rfb1	AXIAL - MF12(4.2X2.0)	10
Electrolytic Capacitor	Cfb1	ECAP-5X2	1.0u
Precision Single Supply Instrumentation Amplifier	Ampb1	DIP-8	AMP04
Resistor	Rb3	AXIAL - RC55(7.2X2.5)	100K
Capacitor	Cb4	CAPACITOR-S100	1.5n
Connector	Jb2	SIP3	CON3
Connector	Jb1	SIP3	CON3
Capacitor	Cb2	CAPACITOR-S100	150p

Version 2 (Figure 6 - middle)

Description	Designator	FootPrint	PartType
Three Terminal Adjustable Current Sources	Us1	TO92B	LM334
Diode	Ds1	D_1N457	1N457
Resistor	Rs2	AXIAL - RC55(7.2X2.5)	130K
Resistor	Rs1	AXIAL - RC55(7.2X2.5)	13K
Capacitor	Cs1	CAPACITOR-S100	0.1u
Electrolytic Capacitor	Cfs2	ECAP-5X2	10u
Capacitor	Cs3	CAPACITOR-S100	0.1u
Resistor	Rfs2	AXIAL - MF12(4.2X2.0)	10
RADFET8 (RADFET in 8-pin DIP package)	FETs1	DIP 8	RADFET8
Resistor	Rfs1	AXIAL - MF12(4.2X2.0)	10
Electrolytic Capacitor	Cfs1	ECAP-5X2	1.0u
Precision Single Supply Instrumentation Amplifier	Amps1	DIP-8	AD623
Capacitor	Cs4	CAPACITOR-S100	1.5n
Connector	Js2	SIP3	CON3
Connector	Js1	SIP3	CON3
Capacitor	Cs2	CAPACITOR-S100	150p

Version 3 (Figure 6 - bottom)

Description	Designator	FootPrint	PartType
Three Terminal Adjustable Current Source	Ut1	TO92B	LM334
Diode	Dt1	D_1N457	1N457
Resistor	Rt2	AXIAL - RC55(7.2X2.5)	130K
Resistor	Rt1	AXIAL - RC55(7.2X2.5)	13K
Capacitor	Ct1	CAPACITOR-S100	0.1u
Electrolytic Capacitor	Cft2	ECAP-5X2	10u
Capacitor	Ct6	CAPACITOR-S100	0.1u
Resistor	Rft2	AXIAL - MF12(4.2X2.0)	10
RADFET8 (RADFET in 8-pin DIP package)	FETt1	DIP 8	RADFET8
Resistor	Rft1	AXIAL - MF12(4.2X2.0)	10
Electrolytic Capacitor	Cft1	ECAP-5X2	1.0u
Precision Single Supply Instrumentation Amplifier	Ampt1	DIP-8	AD820
Capacitor	Ct3	CAPACITOR-S100	1.5n
Connector	Jt2	SIP3	CON3
Connector	Jt1	SIP3	CON3
Capacitor	Ct2	CAPACITOR-S100	150p
Resistor	Rt3	AXIAL - MF12(4.2X2.0)	100k
Resistor	Rt4	AXIAL - MF12(4.2X2.0)	100k
Resistor	Rt5	AXIAL - MF12(4.2X2.0)	100k
Capacitor	Ct4	CAPACITOR-S100	1.5n
Capacitor	Ct5	CAPACITOR-S100	1.5n

The main features of the re-designed board are as follows and are common for all three versions:

- Dimensions were left unchanged, although there is a possibility for further reduction, depending on the actual mission requirements.
- Supply voltage was left unchanged (+12V).
- The main principle of RADFET biasing (continuously supplied positive current), RADFET package type (8-pin DIL package) and voltage readout (RADFET output transferred to the ADC via the operational amplifier) are the same as in the previous design. The nominal gain of the operational amplifier is unity. Voltage reference that existed in the previous version of the board was omitted from the new version.
- Besides the split in the operational amplifier type, two different types of the LM334Z current source package (plastic and metal) were considered, making six the total number of BIOPAN board options. After temperature and irradiation tests, the most suitable types of the operational amplifier and current source package will be chosen for the final board design.
- Instead of surface mounted resistors and diodes in a previous board design, the classic two-lead components were used, for their better temperature stability. The stability of resistors is important as it determines the stability of the biasing current and the gain of the operational amplifier. There is a possibility of switching back to surface mounted components if the temperature stability proves not to be of a major concern.

Figure 7 shows the photograph of the three board versions produced.

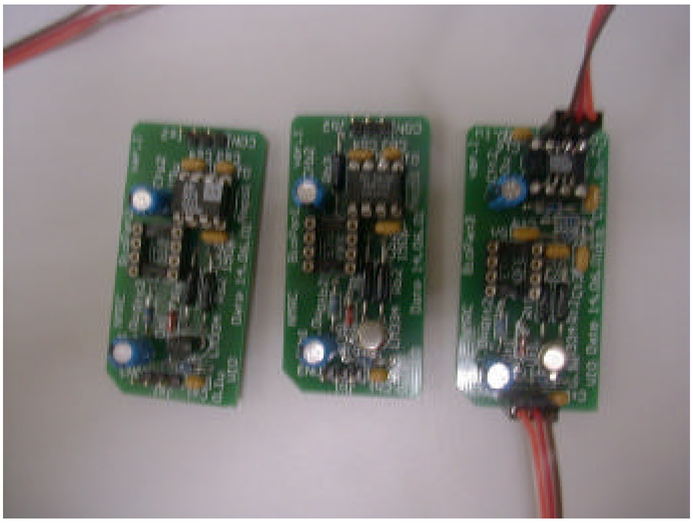

Figure 7: Three re-designed BIOPAN board versions: Version 2, Version 1 and Version 3 (from left to right). Each of the three versions was tested with the LM334Z current source in plastic and metal package, giving the total of six board options. The board on the left has LM334Z in plastic package mounted, while the two boards on the right have LM334Z in metal package. The board on the right has the wires connected via three-way connectors to facilitate electrical tests.

The type of the current source (LM334Z) was left unchanged, as well as the current source configuration with two setting resistors (R_1 and R_2) and the diode. However, a lot of attention was dedicated to tuning the current to a desired 10μA. The tuning was done at the load of R_{load} = 511kΩ, mounted on the board instead of RADFET. The best results (accuracy better than 1%) were achieved for the following values of the setting resistors: R_1 = 9.67kΩ, R_2 = 130kΩ. The load of 511kΩ was chosen as it corresponds to 10μA current biasing the RADFET with the threshold voltage of approximately 5V; this was considered to be in the middle of the RADFET output voltage range. The boards were tested with two other values of the R_{load}: 100kΩ (corresponding to RADFET threshold voltage of approx. 1V) and 825kΩ (corresponding to RADFET threshold voltage of approx. 8V). Table 6 shows the results of the board tests with different values of R_{load}, simulating different RADFET output voltages during the operation of the BIOPAN board in the actual application. Figure 8 plots the RADFET biasing current dependence on R_{load} for all six BIOPAN board options.

Table 6: Results of the electrical tests on six options of the BIOPAN board. The options are related to three different types of the operational amplifier (Opamp 1-3 in board versions 1-3) plus two types of the current source package (plastic or metal). Three different resistor values were used to simulate the RADFETs (evolution of the RADFET output voltage) during board operation in the irradiation field. I is the current value, V_{in} is the input voltage of the operational amplifier (equivalent to the RADFET output voltage), V_{out} is the output voltage of the operational amplifier (output voltage of the board), and K_A is the gain of the operational amplifier.

R_{load} = 100kΩ

Board option	**I (μA)**	**V_{in} (V)**	**V_{out} (V)**	**K_A**
Opamp1, plastic	10.38	1.038	1.045	1.006744
Opamp1, metal	10.43	1.043	1.051	1.007670
Opamp2, plastic	10.35	1.035	1.036	1.000966
Opamp2, metal	10.43	1.043	1.044	1.000959
Opamp3, plastic	10.30	1.030	1.040	1.009709
Opamp3, metal	8.96	0.896	0.905	1.010045

R_{load} = 511kΩ

Board option	**I (μA)**	**V_{in} (V)**	**V_{out} (V)**	**K_A**
Opamp1, plastic	9.96	5.09	5.34	1.049116
Opamp1, metal	10.02	5.12	5.37	1.048828
Opamp2, plastic	9.92	5.07	5.33	1.051282
Opamp2, metal	10.00	5.11	5.37	1.050881
Opamp3, plastic	9.88	5.05	5.31	1.051485
Opamp3, metal	8.61	4.40	4.62	1.050000

R_{load} = 825kΩ

Board option	I (μA)	V_{in} (V)	V_{out} (V)	K_A
Opamp1, plastic	9.68	7.99	8.64	1.081352
Opamp1, metal	9.73	8.03	8.68	1.080946
Opamp2, plastic	9.65	7.96	8.61	1.081658
Opamp2, metal	9.73	8.03	8.69	1.082192
Opamp3, plastic	9.61	7.93	8.58	1.081967
Opamp3, metal	8.38	6.91	7.47	1.081042

It can be seen that the RADFET biasing current is dependent on R_{load}. The reason for this dependence is relatively low impedance of the current source. The accuracy of the current deteriorates as the RADFET output voltage (proportional to R_{load}) shifts from the middle of the operating range towards the lower and upper edges of the range. As mentioned above, the accuracy at 511kΩ is typically better than 1%, and deteriorates to 3-4% at 100Ω and 825kΩ. The current dependence on R_{load} is linear and it may be possible to compensate for current changes.

The K_A dependence on R_{load} is also evident. The K_A accuracy is the best at low RADFET output voltage (R_{load} = 100kΩ) and decreases to some 8% as the output voltage (R_{laod}) increases.

As to the most suitable types of operational amplifier and current source package, from these preliminary tests it seems that, apart from the option (Opamp3, plastic), different options give rather similar results. Clearly, the temperature and radiation tests results will serve as the basis for the choice of the most suitable option.

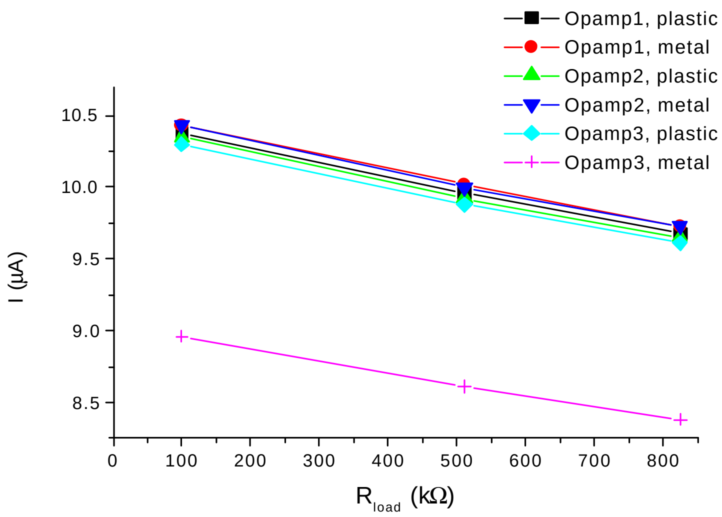

Figure 8: RADFET biasing current dependence on R_{load} for the six different board options.

<u>Work-package 4:</u> Improved Stacked Device

This work-package has not been completed as originally planned. The reasons should be sought in several circumstances, such as recent frequent changes of the NMRC staff members, unexpected delays in the development of the RRB system (crucial task in the whole programme), and, consequently, late commencement of the planned activities. It was estimated that the full realisation of the tasks related to the improved stacked device would take approximately 2 months, including the time needed for the modified stacked device wafers to be fabricated. This was a fairly good estimate, provided that all the prerequisites for device fabrication were in place. Unfortunately, the problem of providing non-standard (low doped) silicon wafers that are used as a starting material for stacked devices has emerged in the meantime and delayed the realisation of the planned work. Fortunately, this work-package is not regarded as the crucial one, the work is not too complicated and could be continued if there was ESTEC requirement to do so.

<u>Work-package 5:</u> High Range/High sensitivity RADFET Configuration

Initial investigation of the possibility of annealing of the radiation-induced damage which would be crucial for the realisation of the high range/high sensitivity RADFET configuration was performed during irradiation campaign in Yugoslavia in December 2000. Experimental samples were irradiated at room temperature with different bias conditions and then annealed at the temperature of 180°C, again with different bias conditions.

The general conclusions from this investigation are as follows:

- The temperature of 180°C is insufficient to fully anneal the radiation-induced damage in the RADFET during reasonably short period of time. Although damage annealing is the most pronounced at early annealing times, within 3-4 days only roughly half of the damage is annealed in the best radiation/annealing bias scenario.
- Even partially annealed RADFETs exhibit decreased radiation sensitivity during the subsequent second irradiation.

As the whole sequence first irradiation/annealing/second irradiation is rather complicated to control and fully characterise even in ideal experimental conditions, it was concluded that the realisation of the proposed RADFET configuration is too ambitious task at this stage of the RADFET development. Nevertheless, the idea is indeed very interesting and might be at least partially revisited in the future.

Appendices

Appendix 1: RADECS 2001 final paper

(presented at 7th Conference on Radiation and its Effects on Devices and Systems – RADECS 2001, 14 – 17 September 2001, Grenoble, France; conference Proceedings in press; paper also accepted for publication in *IEEE Transactions on Nuclear Science*, June issue, 2002)

<u>Appendix 2:</u> MIEL 2002 final paper

(to be presented at the 23rd International Conference on Microelectronics – MIEL 2002, 13 – 16 May 2002, Nis, Yugoslavia)

Appendix 3: Report on PSI Irradiation Campaign in June 2001

Gamma-Ray Irradiation and Post-Irradiation Response of Low Sensitivity/High Dose Range RADFETs

A. Jaksic, G. Ristic, M. Pejovic, A. Mohammadzadeh, C. Sudre, and W. Lane

***Abstract*-- Gamma-ray irradiation and post-irradiation responses have been studied for the two types of radiation sensitive p-channel MOSFETs (RADFETs) from different manufacturers. In addition to, in dosimetric applications standard, threshold voltage measurements at a single specified current, transistor I-V and charge-pumping characteristics have been monitored. This has been shown to be useful in providing a more detailed insight into processes that occur during irradiation and subsequent annealing at elevated temperature. In particular, the role of switching oxide traps (also known as "border" traps) and electron traps in studied devices has been revealed.**

I. Introduction

SINCE the introduction of the space charge dosimeter concept [1], radiation sensitive p-channel MOSFETs (also known as RADFETs) have been developed for applications such as space, nuclear industry and research, and radiotherapy [1-4]. Other types of dosimeters that are commonly used or are being developed for these applications include thermoluminescent dosimeters (TLDs), semiconductor diodes, and optically stimulated luminescence dosimeters (OSDLs). A comprehensive review of radiation dosimetry issues and devices can be found in [5]. The TLDs are rather small, well characterised and standard in use, however, they are not suitable for remote measurements and the read-out of dosimetric information is destructive. Semiconductor diodes are also miniature in size, but produce small dosimetric signal and require high voltage. The OSL dosimetry concept has re-emerged recently with promising results [6,7], however OSLDs require integration of electronics and optic elements in the read-out system and dosmietric information is read destructively. The RADFET advantages include immediate, non-destructive read-out of dosimetric information, extremely small size, very low power consumption, all-electronic interfaces fully compatible with microprocessors, high dose range and very competitive price. The RADFET disadvantages are a need for calibration in different radiation fields, relatively low resolution (starting from about 1 rad) and non-reusability. A new design approach has been investigated recently that could overcome the low resolution problem and introduce the RADFETs into the personnel dosimetry area [8].

The NMRC have been active in RADFET research and development since late 1980's, resulting in a range of commercially available RADFETs for various applications [9], i.e. different dose ranges. This paper will present and discuss the irradiation and post-irradiation response of low sensitivity/high dose range RADFETs. These RADFETs typically have about 100nm thick gate oxides (gate oxide of high sensitivity/low dose range RADFETs can be up to 1 ìm thick) and are suitable for space and nuclear research/industry applications. We will examine the RADFET response in the space dose range, i.e. up to the total absorbed doses of several hundred Gy (1 Gy = 100 rad). The responses of devices from two different manufacturers will be compared.

Radiation induces charge trapping in the gate oxide and at the Si/SiO_2 interface, causing the threshold voltage shift (ΔV_T), which is the RADFET dosimetric parameter. There are several definitions of the MOSFET threshold voltage (V_T) [10], however, the one that is most commonly used in RADFET applications is that the V_T is the voltage needed to sustain a specified current. Thus, the V_T is measured at a single point of the transfer I-V characteristics, applying a specified current (typically in the order of ten ìA) to the RADFET in two-terminal mode (source and bulk are shorted and represent one terminal, while drain and gate are also shorted and represent another terminal). This configuration will be referred to as a Reader Circuit (RC) configuration. While, for its simplicity, the RC configuration is suitable for practical applications and calibration measurements, it doesn't provide the quantification of and insight into the charge trapping mechanisms that could serve as the basis for RADFET fabrication process improvements. For this reason we have performed I-V and charge-pumping (CP) measurements in addition to the RC measurements. This has enabled us to analyse basic mechanisms underlying irradiation and post-irradiation behaviours of the RADFETs and, in particular, discuss the role of switching oxide traps in studied devices.

II. Experimental Details

The RADFETs from two different manufacturers (NMRC, Ireland, and EI-Microelectronics, Yugoslavia)

A. Jaksic, C. Sudre, and W. Lane are with the National Microelectronics Research Centre (NMRC), Cork, Ireland (e-mail of the corresponding author: ajaksic@nmrc.ie).

G. Ristic and M. Pejovic are with the Faculty of Electronic Engineering, University of Nis, Yugoslavia.

A. Moahmmadzadeh is with the ESA/ESTEC, Noordwijk, the Netherlands.

have been investigated. Both types of devices are p-channel MOSFETs fabricated in Al-gate process. The NMRC RADFETs have 100nm thick gate oxide, grown at 1000°C in dry oxygen, and annealed for 15 minutes at 1000°C in nitrogen. The post-metallisation anneal (PMA) was performed at 440°C in forming gas for 60 minutes. The EI RADFETs [11] have 110nm thick gate oxide, grown at 1150°C in wet oxygen, and annealed for 60 minutes at 1050°C in nitrogen. The 30 minute PMA was done at 440°C in forming gas.

Experimental samples were irradiated using the Co-60 source to 300 Gy(H_2O) at the dose rate of 0.013 Gy/s. The gate bias during irradiation (V_{irr}) was either 0 or +5V. Immediately after irradiation, the devices were annealed at 100°C with –10, 0 or +10V annealing bias (V_{ann}). There were at least two (and in many cases more) samples for each annealing experimental condition in terms of V_{irr}/V_{ann} values. The discrepancies between nominally identical samples were in all cases within 5%. The V_T values were determined using the RC configuration with 10 μA current. In addition, device transfer I-V characteristics in saturation were recorded, enabling determination of the "extrapolated" V_T and channel mobility (ì) [10]. The densities of radiation-induced fixed traps (ΔN_{ft}[cm^{-2}]) and switching traps (ΔN_{st}[cm^{-2}]) were determined from the sub-threshold I-V curves using the midgap technique (MGT) of McWhorter and Winokur [12]. Finally, the charge-pumping technique (CPT) measurements [13] were performed to determine the energetic densities of switching traps (ΔD_{st}[$cm^{-2}eV^{-1}$]), $\Delta N_{st}=\Delta D_{st}\times\Delta E$, where ΔE[eV] is an energy range within the Si band-gap scanned by the measurement. Parameters of the CP measurements (recording of Elliot-type CP curves [14], triangular pulse, frequency 100kHz, amplitude 4V, duty cycle 50%) were such that CPT and MGT scanned regions within the silicon band-gap of the same energetic widths (approx. 0.43 eV). Thus, the ΔN_{st} values obtained by MGT and CPT will be directly compared in this paper.

Note that the terms "fixed" and "switching" are used here to define the electrical response of the traps: while fixed traps do not exchange charge with the Si during the time frame of the measurement, switching traps do. Thus, fixed traps cause parallel shift in sub-threshold transfer I-V characteristics (MGT) or Elliot-type CP curves (CPT). Switching traps result in an increase of the sub-threshold slope (MGT) or of the CP current (CPT). As to the location of these traps, fixed traps are located exclusively in the oxide, while switching traps can be exactly at the Si/SiO_2 interface (interface traps, density ΔN_{it}[cm^{-2}]) or in near-interfacial region of the oxide (switching oxide traps, also known as border traps [15], density ΔN_{sot}[cm^{-2}]). Thus, the oxide traps include fixed oxide traps and switching oxide traps, and their total density can be expressed as $\Delta N_{ot}=\Delta N_{ft}+\Delta N_{sot}$. The above described nomenclature was adopted as it better suits the nature of measurements that were done on the experimental samples. Namely, both MG and CP are electrical measurements that can distinguish the radiation-induced defects by their electrical response rather than by location. More details on this will follow in the next Section.

III. Results and Discussion

Figs. 1 and 2 show extrapolated and reader circuit ΔV_T during irradiation for NMRC and EI samples, respectively. The agreement between extrapolated and reader circuit ΔV_T is very good (within 1-2%) in all cases, justifying the use of the RC configuration in practical applications. The radiation sensitivities determined at 300 Gy are given in Table 1.

TABLE I
NMRC AND EI SAMPLES: SENSITIVITY FIGURES
([MV/CGY] AT 300 GY(H_2O))

	V_{irr}=0V	V_{irr}=+5V
NMRC	0.015	0.047
EI	0.071	0.217

The EI samples have roughly a factor of 4.7 higher sensitivity for both V_{irr} conditions. Only a small fraction of the difference can be attributed to somewhat greater oxide thickness of the EI samples (110nm vs. 100nm in the NMRC samples). By far the most of the sensitivity difference comes from charge trapping properties of EI RADFET gate oxide (see below for more details). Note that the high sensitivity may not necessarily be an advantage, particularly in very high dose applications, as it will reduce the maximum detectable dose [2].

Fig. 3 shows the changes in μ, normalised to pre-irradiation value (μ_o), during irradiation. There is almost no change in μ in NMRC samples, while there is a large μ decrease, enhanced by positive V_{irr}, in EI samples.

Figs. 4 and 5 show ΔN_{ft} and ΔN_{st} during irradiation for NMRC and EI samples, respectively. As expected, positive V_{irr} enhances formation of both fixed and switching traps. The MGT and CPT data are in qualitative agreement, but the ΔN_{st}(CPT) is in all cases lower than ΔN_{st}(MGT). The exact quantitative agreement should not be expected for at least two reasons. First, the two techniques have different effective frequencies: a few Hz (MGT) vs. 100kHz (CPT). Both MGT and CPT are capable of sensing the interface traps, which are very fast, but the contributions of switching oxide traps to the CP and MG signals are not the same. While MGT senses almost all switching oxide traps (slow, medium fast and fast), the CP signal in our case excludes at least contributions of slow and medium fast switching oxide traps, and, consequently, ΔN_{st}(CPT) is expected to be lower. Second, the two techniques scan different portions of the Si band gap: lower half (MGT) vs. central portion (CPT). As interface traps have an U-shaped distribution towards the edges of the band gap [10,16] and that portion can not be reached by CPT, this is an additional reason that may lead to the lower ΔN_{st}(CPT) values. The ΔN_{ft} dominates in NMRC samples (at 300 Gy, $\Delta N_{ft}/\Delta N_{st}$ equals 1.9 for V_{irr}=0V, and 3.7 for V_{irr}=+5V). However, in EI samples, ΔN_{st}(MGT) even exceeds ΔN_{ft}. Thus, the greater sensitivity of EI samples is mostly due to the enhanced formation of switching traps (i.e. switching oxide traps and interface traps). It is probable that some portion (NMRC samples) or even most of the ΔN_{ft} determined by MGT (EI samples) is due to switching oxide traps [17] (see discussion further below).

The CPT provides means for estimating not only ΔN_{st}, but also the absolute switching trap densities (N_{st}). The pre-irradiation N_{st} values are $(1.18 \pm 0.03) \times 10^{10}$ cm^{-2}eV^{-1} in NMRC samples, and $(0.42 \pm 0.09) \times 10^{10}$ cm^{-2}eV^{-1} in EI samples. While pre-irradiation N_{st} is higher in the NMRC samples, the fabrication process is better controlled in this respect than the EI one, with much lower N_{st} variations between the samples. The range of N_{st} increase after irradiation in NMRC samples is 4-5 times, while in EI samples it is 30-50 times.

Figs. 6 and 7 show ΔV_T evolution during annealing for NMRC and EI samples, respectively. The ΔV_T behaviour depends primarily on V_{ann}. It is interesting to note that in both samples, the loss of dosimetric information (fading) is more pronounced for zero than for positive V_{ann}.

The μ/μ_o evolution during annealing is shown in Figs. 8 and 9. One of the intentions of our study was to determine the effect of fixed oxide traps on μ in p-channel MOSFETs. Namely, it has been unambiguously established that interface traps have predominant effect on μ, acting to decrease μ in both n-channel and p-channel devices [18,19]. The effect of fixed oxide traps in n-channel devices is qualitatively the same, although quantitatively less pronounced. However, there is still some uncertainty as to whether fixed oxide traps act to decrease or increase μ in p-channel devices. The former is argued by Zupac et al. [20] and has been observed by others as well [21,22]. The latter has been demonstrated by S. Dimitrijev and N. Stojadinovic et al. [23] and attributed to decreased surface-roughness scattering in the presence of fixed oxide traps. In order to confirm one of these models, one has to study p-channel devices in which interface trap creation is negligible in comparison with fixed oxide trap creation. Unfortunately, as the $\Delta N_{ft}/\Delta N_{st}$ ratio is found to be (unexpectedly) high in both types of RADFETs studied here, the predominant effect of ΔN_{st} obscures the effect of ΔN_{ft}. In addition, the contribution of switching oxide traps to ΔN_{st} complicates even quantification of the effects of interface traps on μ. Consequently, no conclusion about ΔN_{ft} effects on μ can be made based on the obtained data. Indeed, it can be seen in Figs. 8 and 9 that μ generally follows the pattern of inverse ΔN_{st} (ΔN_{st} is shown in Figs. 10b-13b).

Figs. 10 and 11 show ΔN_{ft} and ΔN_{st} during annealing for NMRC samples for the case of zero and positive V_{irr}, respectively. The positive V_{ann} enhances formation of switching traps and decay of fixed traps. The ΔN_{ft} even goes into the negative region, particularly in V_{irr}=0V case. Note that there is still a qualitative agreement between ΔN_{st} values obtained by CPT and MGT. Moreover, the changes in ΔN_{st} during annealing as determined by the two techniques are roughly the same.

Finally, Figs. 12 and 13 show the same data as Figs. 10 and 11, but for EI samples. The ΔN_{ft} pattern is qualitatively similar to that in NMRC samples (positive V_{ann} enhances the decrease of ΔN_{ft}). However, there are some quantitative differences, such as larger magnitude of negative ΔN_{ft} observed for both V_{irr}=0 and +5V, particularly in the case of V_{ann}=+10V. As to ΔN_{st}, opposite to the pattern observed in NMRC samples, there is even an absence of ΔN_{st}(MGT) and ΔN_{st}(CPT) qualitative agreement, again particularly for V_{ann}=+10V. Generally, ΔN_{st}(CPT) stays little changed, while ΔN_{st}(MGT) increases substantially (V_{ann}=+10V) or decreases (e.g. V_{irr}=+0V, V_{ann}=-10V in Fig. 12).

Presented experimental results can be most readily explained within the general context of the HDL model [24,25,26]. The crucial role in this model belongs to the $E_{ã}'$ centre, which is a week Si-Si bond in the oxide caused by an oxygen atom vacancy between two Si atoms, each back-bonded to three oxygen atoms [27]. The $E_{ã}'$ centre acts as a hole trap and is predominantly responsible for the increase of oxide trapped charge during irradiation [28]. As discussed in Section II, the oxide trapped charge involves both charge trapped at fixed oxide traps and that trapped at switching oxide traps. Namely, under the influence of the positive electric field in the oxide (caused by positive gate bias) during annealing, the hole trapped at the $E_{ã}'$ centre can be either compensated or neutralised by the electron tunnelling from Si. In the case of compensation, when the negative field (negative gate bias) is applied, the electron can tunnel back to Si, leaving the $E_{ã}'$ centre positively charged. Thus, some of the $E_{ã}'$ centres can communicate electrically with Si, the communication being easier and faster in case they are closer to the Si/SiO_2 interface. We will accept convincing arguments of Lelis and Oldham [26] that the switching oxide traps in irradiated oxides are $E_{ã}'$ centres close to the Si/SiO_2 interface. The fixed oxide traps are microscopically $E_{ã}'$ centres as well, however further from the Si/SiO_2 interface and hence incapable of exchanging charge with Si during the time frame of the measurements.

The negative ΔN_{ft} observed at certain bias conditions in both NMRC and EI samples indicates that there is also negative charge, i.e. electron trapping in the oxide. Such phenomenon has been observed previously in MOSFET oxides and its importance in radiation response demonstrated [29-32]. Electron trapping can also be attributed to $E_{ã}'$ centres [26]. Namely, it has been proposed [33,26] that, under appropriate conditions, the compensated $E_{ã}'$ centre can capture a second electron and become net negative. In other words, after electron capture, $E_{ã}'$ centre becomes an amphoteric trap that can either release or capture an electron and become positively or negatively charged, respectively.

As discussed in Section II, the MGT is a slow technique that registers both interface traps and near-interfacial switching oxide traps ($E_{ã}'$ centres) as switching traps. The much faster CPT registers as switching traps the interface traps and perhaps only the fastest switching oxide traps, i.e. the E_γ' centres closest to the Si/SiO_2 interface that can not be distinguished from interface traps. Thus, the CPT can be used for at least rough estimation of the interface trap behaviour, and. combination of MGT and CPT in some cases may provide information about switching oxide traps.

It is clear that ΔN_{ft}, ΔN_{sot} and ΔN_{it} all increase during irradiation. The exact proportion between ΔN_{sot} and ΔN_{it} during irradiation is difficult to determine, but it is probable that a significant part of ΔN_{st} in NMRC samples and dominant part of ΔN_{st} in EI samples is due to switching oxide traps. This would be in line with observations of Fleetwood et al. [17] in soft oxides.

The ΔN_{ft} behaviour during annealing (Figs. 10a-13a) is consistent with DHL model. For example, for V_{ann}=-10V, ΔN_{ft} increases (V_{irr}=0V) or decreases slightly (V_{irr}=+5V) in both NMRC and EI samples. The increase for V_{irr}=0V is due to tunnelling of trapped holes from E_γ' centres to Si under the influence of negative electric field at the Si/SiO_2 interface. The slight decrease for V_{irr}=+5V indicates that the built-in positive field in the vicinity of the interface due to radiation-induced positive charge is stronger than the negative filed caused by V_{ann}, enabling the electrons to tunnel from Si to E_γ' centres and neutralise the holes trapped there. As expected, much more pronounced ΔN_{ft} decrease is observed for V_{ann}=0 and +10V, which both correspond to the positive electric field at the Si/SiO_2 interface, the field being greater in magnitude in the latter case and hence ΔN_{ft} decrease enhanced. Besides neutralisation of charge trapped at E_γ' centres by electrons tunnelling from Si under the influence of electric field, the electrons thermally emitted from the oxide valence band also contribute to E_γ' centres neutralisation [34]. Finally, electron trapping is another mechanism causing ΔN_{ft} decrease. Electron trapping is more pronounced in EI samples, and, as expected, for positive V_{ann}.

If we consider ΔN_{st} behaviour during annealing (Figs. 10b-13b), in NMRC samples there is ΔN_{st}(MGT) increase closely followed by ΔN_{st}(CPT) increase. The parallel offset between ΔN_{st}(MGT) and ΔN_{st}(CPT) implies that there is a genuine increase in interface traps during annealing and that the number of switching oxide traps stays roughly unchanged. This is consistent with previous results by Fleetwood et al. [17]. The build-up of interface traps during irradiation and annealing can be explained by the so called hydrogen models [16], which involve release of hydrogenous species in the oxide, their transport to the Si/SiO_2 interface and reactions in which interface traps are formed. According to hydrogen models, details of interface traps behaviour are determined by the hydrogen content of the oxide and V_{ann} (both increased hydrogen content and positive V_{ann} enhance formation of interface traps). Interface trap models will not be elaborated in detail here, the reader is referred to the original work [35,36].

In EI samples, ΔN_{st}(CPT) is roughly constant during annealing, implying that there is little or no change in ΔN_{it}, and, hence, ΔN_{st}(MGT) behaviour approximates that of ΔN_{sot}. For V_{ann}=+10V, similar to NMRC samples, there is a substantial increase in ΔN_{st}(MGT). However, in contrast to NMRC samples, ΔN_{st}(MGT) increase is due to switching oxide traps, and not interface traps. The patterns of ΔN_{ft}, ΔN_{sot} and ΔN_{it} behaviours during annealing with V_{ann}=+10V are summarised in Table 2.

TABLE II

NMRC AND EI SAMPLES: ΔN_{FT}, ΔN_{SOT} AND ΔN_{IT} PATTERNS DURING ANNEALING WITH V_{ANN}=+10V.

	ΔN_{ft}	ΔN_{it}	ΔN_{sot}
NMRC			
EI			

For V_{ann}=-10V, there is a decrease in ΔN_{st}(MGT). The decrease is more pronounced in the case of V_{irr}=0V than V_{irr}=+5V, most probably because the resultant field at the Si/SiO_2 interface is more negative in the former case owing to less positive charge trapped (compare ΔN_{ft} in Figs. 12a and 13a). For an intermediate case of V_{ann}=0V, initial increase in ΔN_{st}(MGT) is followed by a decrease at later annealing times. The turn-around point is at the time when the electric field at the Si/SiO_2 interface, primarily determined by the sign of ΔN_{ft}, turns negative (see e.g. Fig. 13b). It seems that in EI samples the electric field at the interface determines switching oxide traps behaviour: positive field acts to increase ΔN_{sot}, while negative field acts to decrease ΔN_{sot}. This can be explained by assuming that tunnelling of electrons from Si to the E_γ' centres under the positive bias results in creation of switching oxide traps. Oppositely, tunnelling of electrons from E_γ' centres to Si leaves the centres in the state in which they cannot exchange charge with Si during the measurements. Microscopically, all these defects are related to the E_γ' centres, but the capture or release of electron changes the energy level and thereby the nature of the centre. Physical location of the centres and their energy levels may be differ from oxide to oxide, causing different radiation responses as observed in our study.

Differences in details of the radiation response of NMRC and EI samples (see e.g. Table 2) are the consequence of different parameters of processing steps used during fabrication of experimental samples. It is not easy to unambiguously determine which particular process step is crucial for the explanation of the radiation response, as the response is often determined not only by the individual step, but by the process sequence within which it occurs [16]. Nevertheless, general impact of certain steps has been documented and can be analysed. Thus, the lower post-process ΔN_{st} in NMRC samples is probably the consequence of, among other things, longer PMA time in these samples compared to EI ones.

As E_γ' centres are argued to have a dominant role in hole and electron trapping at both fixed or switching traps in the oxides investigated here, we will discuss the process steps crucial for E_γ' centres formation. It has been shown [37] that the formation of E_γ' centres is predominantly affected by the highest temperature used in the process flow. In our case of Al-gate devices it is the oxidation temperature. In addition, the post-oxidation anneal (PMA) step has been shown to be of the most importance for the switching oxide trap behaviour. Both oxidation and POA were performed at higher temperatures in EI samples, and the POA duration was longer as well. Increased oxidation temperature, POA temperature and POA duration all act to increase the number of $E_{\tilde{a}}'$ centres in the oxide [38,39]. This may be the explanation for higher radiation sensitivity due to increased charge trapping in EI samples, as well as for generally more pronounced changes in ΔN_{ft} and ΔN_{st} during annealing. On the other hand, it has been argued [37-39] that the higher temperature POA relieves the strain in the vicinity of the Si/SiO_2 interface. Within the context of DHL model, relieved strain leads to the smaller number of $E_{\tilde{a}}'$ centres that act as switching oxide traps, while it doesn't necessarily mean smaller total number of $E_{\tilde{a}}'$ centres [26,40]. Such oxides would exhibit slower decay of ΔN_{ft} during annealing [40], which is not observed in our case. Perhaps the reason for this discrepancy is in the complex influence of not only individual process steps but also certain process sequences on location and energy levels of the traps in the oxide. The problem is also in the inability of the employed characterisation techniques to provide information about some pertinent details of the microscopic processes that occur during irradiation and annealing. For example, it still cannot be distinguished by CPT with complete certainty whether the ΔN_{it} increase in NMRC samples (Figs. 10b and 11b) is really entirely due to interface traps or to switching oxide traps very near the Si/SiO_2 interface. Similarly, the effects of hole and electron trapping are both contained in ΔN_{ft} data and cannot be separated using MGT.

IV. Conclusions

Radiation and post-irradiation responses of the two types of low sensitivity/high dose range RADFETs have been investigated. Measurements in practical applications and during RADFET calibration typically involve determination of the threshold voltage only in a single specified point of the device I-V characteristic. While such procedure is confirmed to be sufficient from the application point of view, RADFET further development requires insight into microscopic processes that occur during irradiation and subsequent annealing. This study has demonstrated the use of sub-threshold midgap and charge pumping techniques in RADFETs. Admittedly, these electrical techniques have limitations, such as that they cannot provide information of the microscopic structure of the defects in the oxide and at the Si/SiO_2 interface, or cannot clearly distinguish the contributions of electrons and holes to the charge trapped in the oxide. However, concurrent use of MGT and CPT can provide information about the effects of switching oxide traps and interface traps, which are indistinguishable when a single technique (e.g. MGT is used). The knowledge about behaviour patterns of interface traps, switching oxide traps, together with that of fixed oxide traps, is crucial in optimising the RADFET response. Often complex interplay between these three types of traps determines radiation sensitivity and post-irradiation stability (fading). That explains, for instance, somewhat unexpected result in Figs. 6 and 7 that fading is lower for V_{ann}=+10V than for V_{ann}=0V. (It is expected that the fading for V_{ann}=-10V is the lowest.) Switching oxide traps are particularly important in RADFETs as they have the dominant influence on another important parameter – a short-term drift [41].

It has been proposed that the $E_{\tilde{a}}'$ centres play the crucial role in RADFET response, being responsible for both fixed and switching traps in the oxide and for both hole and electron trapping. Therefore, the need to optimise the RADFET fabrication process in terms of $E_{\tilde{a}}'$ centres number, location and energy is of paramount importance. This can be done by optimisation of the highest temperature processes, i.e. usually gate oxidation and subsequent anneal in an inert atmosphere. However, one should be careful when making conclusions because sometimes the whole process sequence rather than individual process steps can have an impact on radiation and post-irradiation response of the devices.

V. References

[1] A. Holmes-Siedle, *Nucl. Instrum. Methods*, vol. 121, p. 169, 1974.
[2] A. Holmes-Siedle and L. Adams, *Radiat. Phys. Chem.*, vol. 28, p. 235, 1986.
[3] A. Kelleher et al., *Sensors and Actuators A*, vol. 37, p. 370, 1993.
[4] D.J. Gladstone et al., *Med. Phys.*, vol. 21, p. 1721, 1994.
[5] G.F. Knoll, Radiation detection and measurement, New York: Wiley, 1989.
[6] G. Polge et al., Paper A-1 at RADECS 2001, Grenoble.
[7] D. Plattard et al., Paper A-2 at RADECS 2001, Grenoble.
[8] B. O'Connell et al., *IEEE Trans. Nucl. Sci.*, vol. 45, p. 235, 1998, and references therein.
[9] www.nmrc.ie/projects/radfets/index.html
[10] S.M. Sze, Physics of Semiconductor Devices, New York: Wiley, 1981.
[11] G. Ristic et al., *Sensors and Actuators A*, vol. 63, p. 129, 1997, and references therein.
[12] P.J. McWhorter and P.S. Winokur, *Appl. Phys. Lett.*, vol. 48, p. 133, 1986.
[13] G. Groeseneken et al., *IEEE Trans. Electron Dev.*, vol. 31, p. 42, 1984.
[14] A.B.M. Elliot, Solid-State Electron., vol 19, p. 241, 1976.
[15] D.M. Fleetwood, *IEEE Trans. Nucl. Sci.*, vol. 39, p. 269, 1992.
[16] T.P. Ma and P.V. Dressendorfer, Ionizing radiation effects in MOS devices and circuits, New York: Wiley, 1989.
[17] D.M. Fleetwood, *IEEE Trans. Nucl. Sci.*, vol. 44, no. 6, p. 1810-1817, 1997.
[18] K.F. Galloway et al., *IEEE Trans. Nucl. Sci.*, vol. 31, p. 1497, 1984.
[19] D.M. Fleetwood et al., *IEEE Trans. Nucl. Sci.*, vol. 36, p. 1816, 1989.
[20] D. Zupac et al., *IEEE Trans. Nucl. Sci.*, vol. 40, p. 1307, 1993, and references therein.
[21] F.B. McLean and H.E. Boesch, Jr., *IEEE Trans. Nucl. Sci.*, vol. 36, p. 1772, 1989.
[22] N.S. Saks et al., *IEEE Trans. Nucl. Sci.*, vol. 35, p. 1234, 1988.
[23] S. Dimitrijev and N. Stojadinovic, *Solid-State Electron.*, vol. 30, p. 991, 1987.
[24] A.J. Lelis et al., *IEEE Trans. Nucl. Sci.*, vol. 35, p. 1186, 1988.
[25] A.J. Lelis et al., *IEEE Trans. Nucl. Sci.*, vol. 36, p. 1808, 1989.
[26] A.J. Lelis and T.R. Oldham, *IEEE Trans. Nucl. Sci.*, vol. 41, p. 1835, 1994.
[27] F.J. Feigl et al., *Solid-State Commun.*, vol. 14, p. 225, 1974.
[28] P.M. Lenahan and P.V. Dressendorfer, *J. Appl. Phys.*, vol. 55, p. 3495, 1984.
[29] D.M. Fleetwood et al., *J. Appl. Phys.*, vol. 73, p. 5058, 1993.
[30] V.S. Pershenkov et al., *IEEE Trans. Nucl. Sci.*, vol. 42, p. 1750, 1995.
[31] V.S. Pershenkov et al., *IEEE Trans. Nucl. Sci.*, vol. 43, p. 2579, 1996.
[32] D.M. Fleetwood et al., *IEEE Trans. Nucl. Sci.*, vol. 46, p. 1519, 1999.
[33] M. Walters and A. Reisman, *J. Electrohem. Soc.*, vol. 138, p. 2756, 1991.

[34] P.J. McWhorter et al., *IEEE Trans. Nucl. Sci*., vol. 37, p. 1682, 1990.
[35] D.B. Brown and N.S. Saks, *J. Appl. Phys*., vol. 70, p. 3734, 1991, and the reference therein.
[36] R.E. Stahlbush et al., *J. Appl. Phys*., vol. 73, p. 658, 1993, and the reference therein.
[37] P.M. Lenahan et al., *IEEE Trans. Nucl. Sci*., vol. 46, p. 1534, 1999.
[38] J.R. Schwank and D.M. Fleetwood, *Appl. Phys. Lett*., vol. 64, p. 770, 1988.
[39] W.L. Warren et al., *Appl. Phys. Lett*., vol. 53, p. 3452, 1994.
[40] T.R. Oldham et al., *IEEE Trans. Nucl. Sci*., vol. 33, p. 1203, 1986.
[41] Z. Savic et al., *IEEE Trans. Nucl. Sci*., vol. 42, p. 1445, 1995.

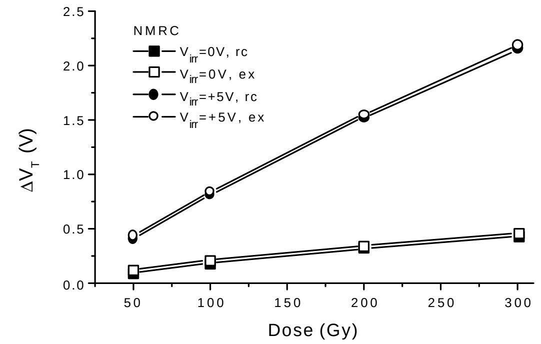

Fig. 1. NMRC samples: reader circuit (rc) and extrapolated (ex) ΔV_T during irradiation with zero and positive gate bias.

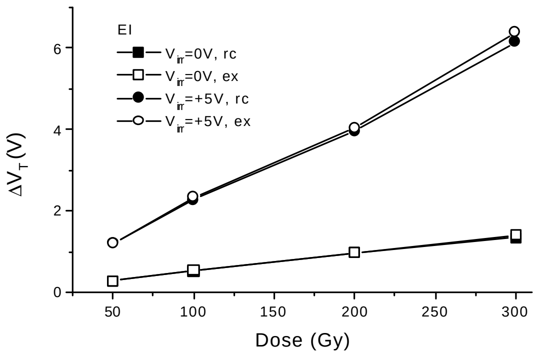

Fig. 2. EI samples: reader circuit (rc) and extrapolated (ex) ΔV_T during irradiation with zero and positive gate bias.

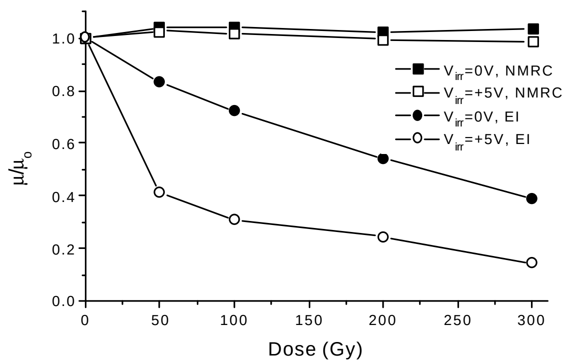

Fig. 3. NMRC and EI samples: μ/μ_o during irradiation with zero and positive gate bias.

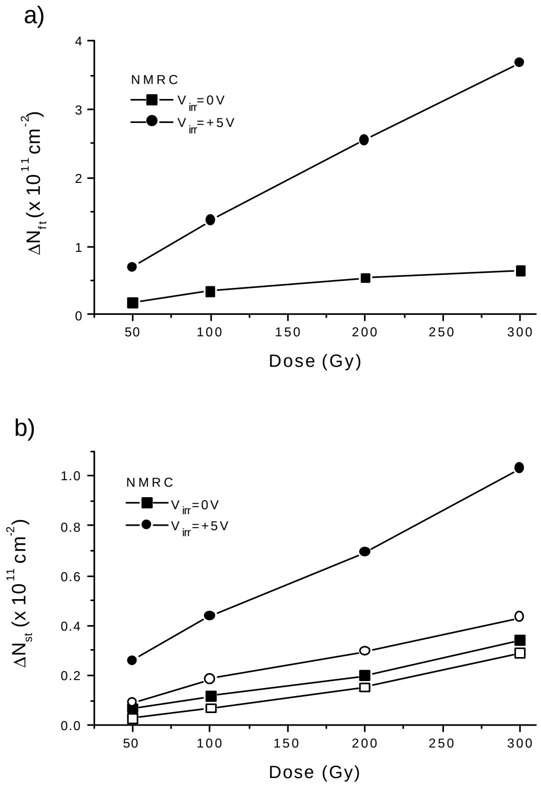

Fig. 4. NMRC samples: ΔN_{ft} (a) and ΔN_{st} (b; MG-solid symbols, CP-open symbols) during irradiation with zero and positive gate bias.

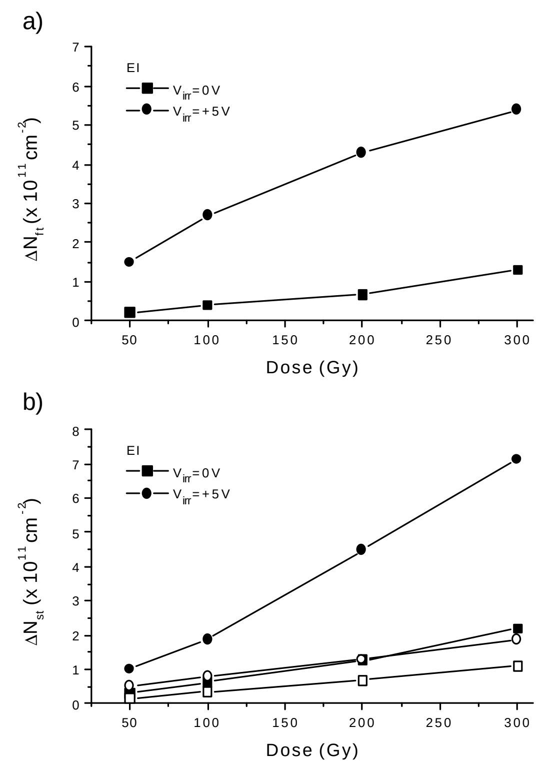

Fig. 5. EI samples: ΔN_{ft} (a) and ΔN_{st} (b; MG-solid symbols, CP-open symbols) during irradiation with zero and positive gate bias.

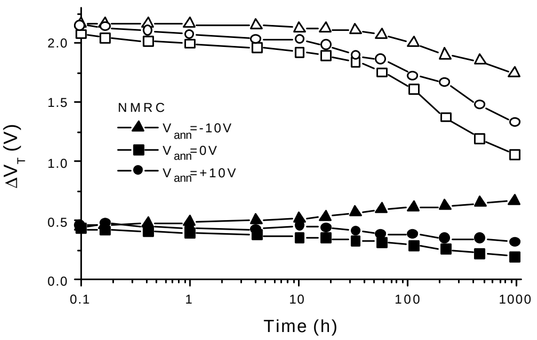

Fig. 6. NMRC samples: ΔV_T during annealing at 100°C with negative, zero and positive gate bias; solid symbols - zero irradiation bias, open symbols - positive irradiation bias (+5V).

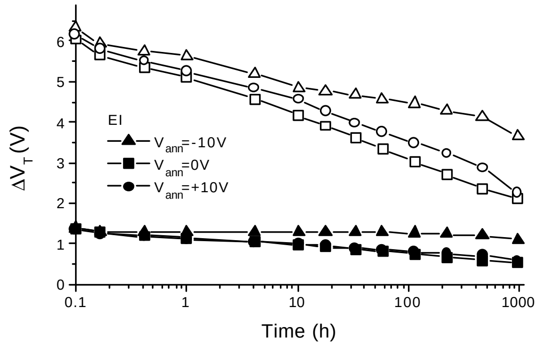

Fig. 7. EI samples: ΔV_T during annealing at 100°C with negative, zero and positive gate bias; solid symbols - zero irradiation bias, open symbols - positive irradiation bias (+5V).

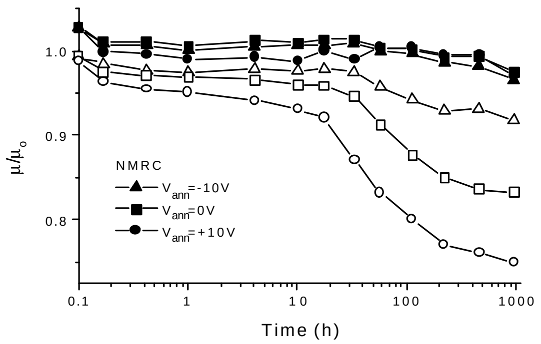

Fig. 8. NMRC samples: μ/μ_o during annealing at 100°C with negative, zero and positive gate bias; solid symbols - zero irradiation bias, open symbols - positive irradiation bias (+5V).

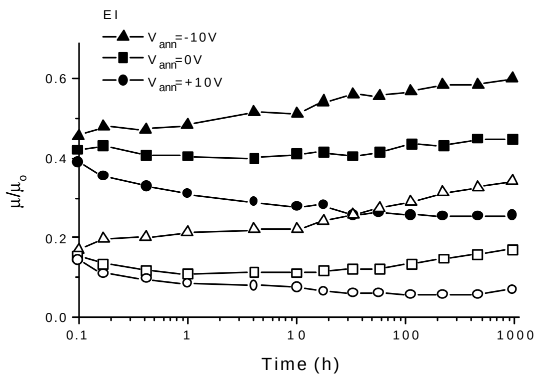

Fig. 9. EI samples: μ/μ_o during annealing at 100°C with negative, zero and positive gate bias; solid symbols - zero irradiation bias, open symbols - positive irradiation bias (+5V).

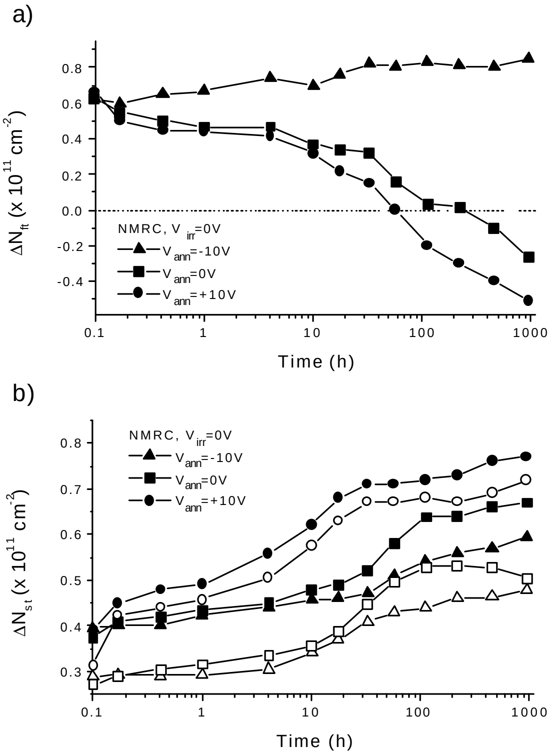

Fig. 10. NMRC samples: ΔN_{ft} (a) and ΔN_{st} (b; MG-solid symbols, CP-open symbols) during annealing at 100°C with negative, zero and positive gate bias; zero irradiation bias.

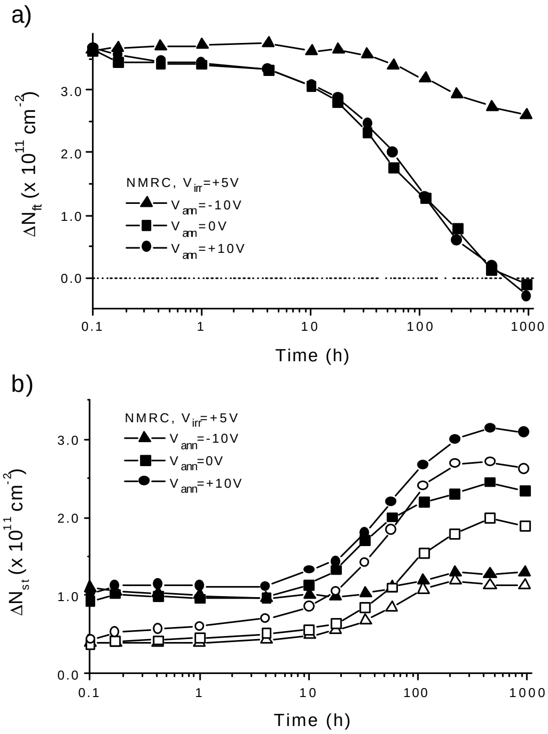

Fig. 11. NMRC samples: ΔN_{ft} (a) and ΔN_{st} (b; MG-solid symbols, CP-open symbols) during annealing at 100°C with negative, zero and positive gate bias; positive irradiation bias (+5V).

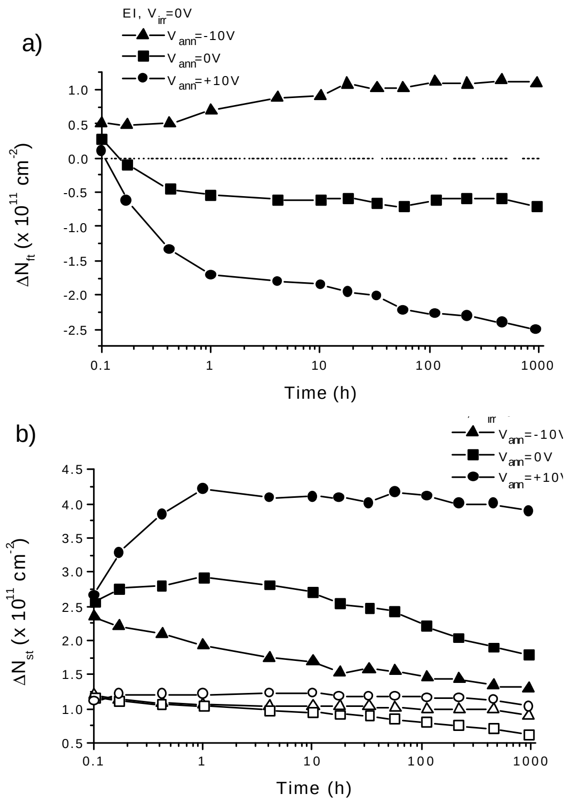

Fig. 12. EI samples: ΔN_{ft} (a) and ΔN_{st} (b; MG-solid symbols, CP-open symbols) during annealing at 100°C with negative, zero and positive gate bias; zero irradiation bias.

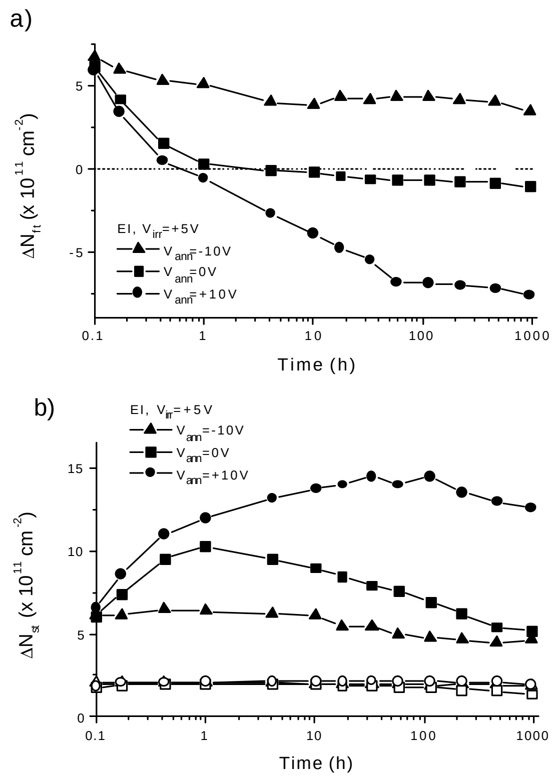

Fig. 13. EI samples: ΔN_{ft} (a) and ΔN_{st} (b; MG-solid symbols, CP-open symbols) during annealing at 100°C with negative, zero and positive gate bias; positive irradiation bias (+5V).

Characterisation of Radiation Response of 400nm Implanted Gate Oxide RADFETs

A. Jaksic, G. Ristic, M. Pejovic, A. Mohammadzadeh, and W. Lane

Abstract – In order to achieve lower initial threshold voltage, a boron implantation has been done through thermally grown 400nm gate oxide of the radiation sensitive p-channel MOSFET (RADFET). The paper presents and discusses the results of a recent study aimed to provide detailed characterisation of radiation response of this type of RADFET. Implications of the implantation for practical RADFET applications and basic mechanisms underlying device radiation behaviour are analysed.

I. INTRODUCTION

Since the introduction of the space charge dosimeter concept [1], radiation sensitive p-channel MOSFETs (also known as RADFETs) have been developed for applications such as space, nuclear industry and research, and therapy [1]-[4]. RADFET advantages include immediate, non-destructive read out, extremely small size, very low power consumption, compatibility with microprocessors, and competitive price (especially if cost of the read out system is taken into account). The NMRC have been active in RADFET research and development since late 1980's, resulting in a range of commercially available RADFETs for various applications [5]. The most popular among the NMRC standard RADFET types is 400nm implanted gate oxide device (here referred to as 400nm IMPL RADFET). This paper will present and discuss the results of a recent study aimed to provide detailed characterisation of radiation response of 400nm IMPL RADFET. Basic mechanisms underlying device radiation behaviour will be analysed.

II. EXPERIMENTAL DETAILS

The recently improved NMRC 400nm IMPL RADFET chip contains two types of devices, differing in W/L ratio: 300/50 and 690/15 (W – channel width, L – channel length, both in ìm). The gate oxide of both types is 400nm thick, grown in dry oxygen and annealed in nitrogen. Boron implantation is done through the oxide to reduce the initial, pre-irradiation threshold voltage (V_{T0}). Thus, from V_{T0} of around –8V for a similar unimplanted device, V_{T0} is decreased to about –2V (300/50 RADFET). The V_{T0} is further decreased in 690/15 implanted gate oxide device to about –0.5V. Due to creation of additional defects in the oxide during implantation, radiation sensitivity of 400nm IMPL RADFET is enhanced several-fold in comparison with an unimplanted gate oxide counterpart. However, for the same reason, the long-term stability (also known as "fading") is somewhat degraded.

Experimental samples were irradiated using the Co-60 source to 50 Gy(H_2O) (1Gy=100rad) at the dose rate of 0.013 Gy/s. The gate bias during irradiation (V_{irr}) was either -5, 0 or +5V. There is a large database of calibration measurements done on 300/50 400nm IMPL RADFETs, however this includes mostly threshold voltage measurements in one point of the I-V transfer characteristics, in the so called Reader Circuit (RC) configuration (see Fig. 1). There have been no measurements on a newly introduced 690/15 device. Further, the RC measurements do not provide an insight into radiation-induced defects in the gate oxide and at the Si/SiO_2 interface.

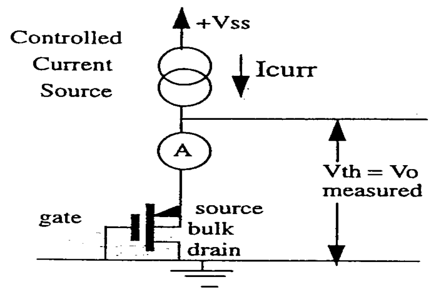

Fig. 1. Reader Circuit (RC) configuration for threshold voltage measurements in RADFETs; Icurr=10ìA.

These were the reasons why a detailed 400nm IMPL RADFET radiation response characterisation study was performed. In addition to the RC threshold voltage (V_T) measurements, device above-threshold and sub-threshold transfer characteristics in saturation were recorded, enabling determination of the "extrapolated" V_T and channel carrier mobility (ì) [6] and of the densities of

A. Jaksic is with the National Microelectronics Research Centre (NMRC), Lee Maltings, Prospect Row, Cork, Republic of Ireland, E-mail: ajaksic@nmrc.ie

G. Ristic is with the Sunnybrook Health Science Centre, University of Toronto, 2075 Bayview Avenue, Toronto, Canada, E-mail: gristic@sten.sunnybrook.utoronto.ca

M. Pejovic is with the Faculty of Electronic Engineering, University of Nis, Beogradska 14, 18000 Nis, Yugoslavia, E-mail: pejovic@elfak.ni.ac.yu

A. Mohammadzadeh is with the European Space Agency (ESA-ESTEC), PO Box 299, Noordwijk, The Netherlands, E-mail: ali.mohammadzadeh@esa.int

W. Lane is with Analog Devices, Airport Business Park, Cork, Republic of Ireland, E-mail: bill.lane@analog.com

radiation-induced oxide-trapped charge (ΔN_{ot}[cm^{-2}]) and interface traps (ΔN_{it}[cm^{-2}]), using midgap technique (MGT) of McWhorter and Winokur [7].

III. Results and Discussion

Fig. 2 shows extrapolated and RC ΔV_T during irradiation. The agreement between extrapolated and RC ΔV_T is very good (within 1-2%) in all cases, justifying the use of a very simple RC measurement configuration in practical applications. The radiation sensitivity figures at different doses are given in Table 1.

TABLE I
Radiation sensitivity figures ([mV/cGy], 300/50 RADFET, RC configuration)

Dose (Gy)\\V_{irr}	V_{irr}=-5V	V_{irr}=0V	V_{irr}=+5V
1	0.28	0.82	1.56
10	0.26	0.72	1.46
50	0.22	0.50	1.27

As expected, sensitivity decreases with dose, such a sub-linear response being typical of RADFETs [1],[2]. The sensitivity at negative V_{irr} is lower than at zero bias, which is not always the case [8]. Such behaviour is connected to the trapping properties of the oxide. In the 400nm IMPL oxide, a benefit to sensitivity of decreased initial recombination or radiation-induced electron-hole pairs that comes from non-zero bias is offset by the location of trapped positive charge further from the Si/SiO_2 interface that comes with negative V_{irr}. In some samples the former effect dominates, leading to a higher sensitivity for negative than for zero V_{irr}; see [8] for more details. It is worth noting that the spread of sensitivity values between nominally identical samples is very favourable. Namely, the RADFETs may suffer from problems in controlling the fabrication process steps, particularly thick gate oxide growth. Up to 8 nominally identical samples were tested for each V_{irr} and the mean variation of sensitivities was found not to exceed 2% in all cases.

Fig. 3 shows the effect of W/L ratio on radiation response. It can be seen that W/L doesn't have a great influence on radiation sensitivity: 690/15 device is typically only 1-2% less sensitive that 300/50 one. This is a promising result, as for its low V_{T0} 690/15 device is suitable for applications where the output voltage range is limited. Namely, as the RADFET threshold voltage increases during irradiation, at some stage it may exceed the supply voltage of the RADFET read-out circuit employed in practical application (in principle, read-out circuits are based on RC configuration in Fig. 1), resulting in circuit malfunction. Lower V_{T0} would basically mean higher dose range that can be detected by the circuit.

Fig. 4 shows ΔN_{ot} and ΔN_{it} during irradiation. The scales of vertical axes in Figs. 4a and 4b are the same, enabling comparison between ΔN_{ot} and ΔN_{it}. For all bias conditions, the positive bias enhances and the negative bias suppresses formation of oxide-trapped charge and interface traps, at least as measured by MGT. The ΔN_{ot} is in all cases greater than ΔN_{it}; see Table 2 for exact quantification.

TABLE II
$\Delta N_{OT}/\Delta N_{IT}$ ratio for negative, zero and positive bias (50Gy dose, 300/50 RADFET, RC configuration)

	V_{irr}=-5V	V_{irr}=0V	V_{irr}=+5V
$\Delta N_{ot}/\Delta N_{it}$	4.93	2.87	2.59

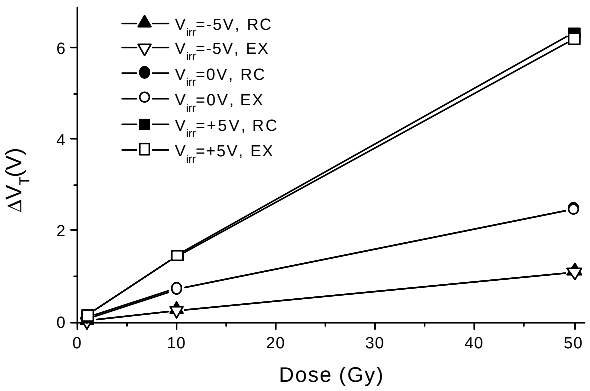

Fig. 2. Reader Circuit (RC) and extrapolated (EX) ΔV_T during irradiation with negative, zero and positive gate bias.

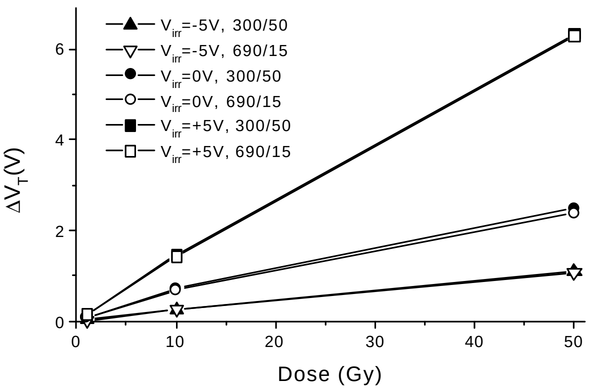

Fig. 3. ΔV_T during irradiation with negative, zero and positive gate bias for RADFETs with different W/L; W and L in ìm.

The $\Delta N_{ot}/\Delta N_{it}$ ratio is unexpectedly low, i.e. ΔN_{it} formation is more pronounced than expected. It is typical to assume that the interface trap formation in RADFETs is negligible in comparison with oxide-trapped charge buildup [1],[2]. Explanation for the effect observed here may be sought in an important role of the switching oxide traps [9], also known as border traps [10]. Switching oxide traps are physically located in the oxide, but electrically behave as interface traps, i.e. can exchange charge with the silicon substrate within the framework of the employed measurement. If the traps are very close to the Si/SiO_2 interface, they cannot be distinguished from interface traps, particularly by slow measurement techniques, such as MGT. It may be that the ΔN_{it} in Fig. 4b in fact predominantly contains information about switching oxide traps, rather than about "true" interface traps, located exactly at the Si/SiO_2 interface. In that case, ΔN_{ot} would not represent density of all hole traps located in the oxide, but only of those hole traps that cannot exchange charge with the silicon within the framework of the measurement (the so called fixed oxide traps). It should be noted that, besides the existence of switching oxide traps, a part of observed ΔN_{it} may be due to the charge lateral non-uniformities (LNUs).

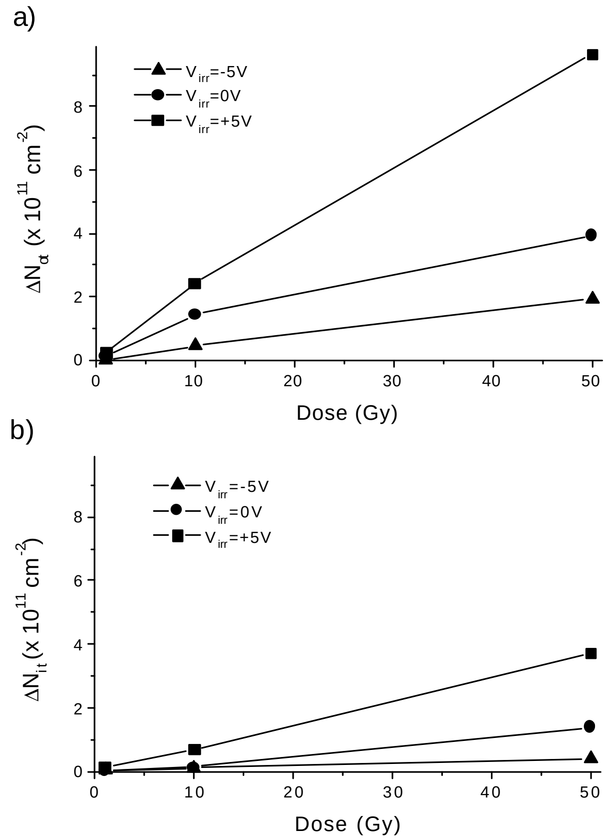

Fig. 4. ΔN_{ot} (a) and ΔN_{it} (b) determined by MGT during irradiation with negative, zero and positive gate bias.

The μ/μ_o evolution during irradiation is shown in Fig. 5. The μ decreases during irradiation in all cases, the decrease being enhanced by V_{irr}. One of the intentions of our study was to determine the effect of oxide-trapped charge on μ in p-channel MOSFETs. Namely, it has been unambiguously established that interface traps have predominant effect on μ, acting to decrease μ in both n-channel and p-channel devices. The effect of oxide-trapped charge in n-channel devices is qualitatively the same, although quantitatively less pronounced. However, there is still some uncertainty as to whether oxide-trapped charge acts to decrease or increase μ in p-channel devices. The former is argued by Zupac et al. [11], and latter has been demonstrated by N. Stojadinovic et al. [12] and attributed to decreased surface roughness scattering in the presence of oxide-trapped charge. In order to confirm one of these models, one has to study p-channel devices in which interface trap creation is negligible in comparison with oxide-trapped charge creation. Unfortunately, as the $\Delta N_{ot}/\Delta N_{it}$ ratio is found to be (unexpectedly) high in the RADFETs studied, the predominant effect of ΔN_{it} obscures the effect of ΔN_{ot}. In addition, the contribution of switching oxide traps to ΔN_{it} complicates even quantification of the effects of interface traps on μ. Consequently, no conclusion about ΔN_{ot} effects on μ can be made based on the obtained data. Indeed, it can be seen in Fig. 5 that μ generally follows the pattern of inverse ΔN_{it} (ΔN_{it} is shown in Fig. 4b).

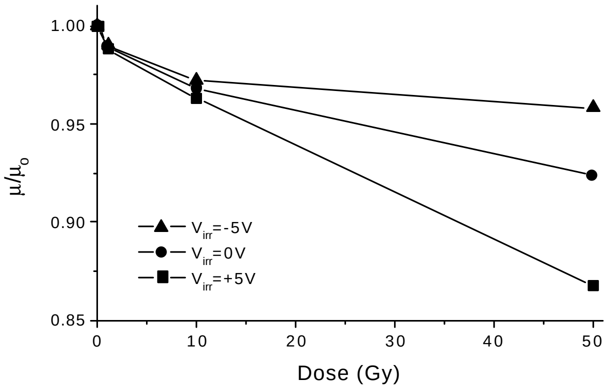

Fig. 5. Ratio μ/μ_o during irradiation with negative, zero and positive gate bias.

IV. Conclusions

Presented experimental results, together with those in another recent study [13], suggest an important role of the switching oxide traps in investiagated RADFETs, while the influence of charge lateral non-uniformities should also be taken into account. There is evidence that switching oxide traps can be attributed exclusively to the E' centres in the oxide [9], although others argue that there two different types of defects play a role [14]. It seems to us that the arguments in [9] are rather convincing; but the electrical MGT technique used in our study cannot provide any evidence of the microscopic nature of the defect in the gate oxide and at the Si/SiO_2 interface.

Ion implantation after the gate oxide growth indeed induces additional defects in the RADFET gate oxide. Initial results (not shown here) indicate that this has an adverse effect on post-irradiation characteristics of the implanted gate oxide RADFETs. However the gains in radiation sensitivity and broader measurable dose range due to decreased initial threshold voltage fully justify application of the additional implantation step.

References

[1] A. Holmes-Siedle, "The Space-Charge Dosimeter", *Nucl. Instrum. Methods*, vol. 121, pp. 169-179, 1974.

[2] A. Holmes-Siedle and L. Adams, "RADFET: A Review of the Use of Metal-Oxide-Silicon Devices as Integrating

Dosimeters", *Radiat. Phys. Chem.*, vol. 22, pp. 235-244, 1986.

[3] A. Kelleher, N. McDonnell, B. O'Neill, L. Adams and W. Lane, "The Effect of Gate Oxide Process Variations on the Long-Term Fading of the PMOS Dosimeters", *Sensors and Actuators A*, vol. 37-38, pp. 370-374, 1993.

[4] D.J. Gladstone, X.Q. Lu, J.L. Humm, H.F. Bowman, and L.M. Chin, "Miniature MOSFET Radiation Dosimeter Probe", *Med. Phys.*, vol. 21, pp. 1721-1728, 1994.

[5] www.nmrc.ie/projects/radfets/index.html

[6] S.M. Sze, *Physics of Semiconductor Devices*, New York, Wiley, 1981.

[7] P.J. McWhorter and P.S. Winokur, "Simple Technique for Separating the Effects of Interface Traps and Trapped-Oxide Charge in Metal-Oxide-Semiconductor Transistors", *Appl. Phys. Lett*., vol. 48, pp. 133-135, 1986.

[8] G. Ristic, M. Pejovic, and A. Jaksic, "PMOS Dosimetric Transistors with Two-Layer Gate Oxide", *Sensors and Actuators A*, vol. 63, pp. 129-134, 1997, and references therein.

[9] A.J. Lelis and T.R. Oldham, "Time Dependence of Switching Oxide Traps", *IEEE Trans. Nucl. Sci*., vol. 41, pp. 1835-1843, 1994, and references therein.

[10] D.M. Fleetwood, "Border Traps in MOS Devices", *IEEE Trans. Nucl. Sci*., vol. 39, pp. 269-271, 1992.

[11] D. Zupac, K.F. Galloway, P. Khosropour, S.R. Anderson, and R.D. Schrimpf, "Separation of the Effects of Oxide-Trapped Charge and Interface-Trapped Charge on Mobility in Irradiated Power MOSFETs", *IEEE Trans. Nucl. Sci.*, vol. 40, pp. 1307-1315, 1993, and references therein.

[12] N. Stojadinovic, M. Pejovic, S. Golubovic, G. Ristic, V. Davidovic, and S. Dimitrijev, "Effect of Radiation-Induced Oxide-Trapped Charge on Mobility in p-Channel MOSFETs", *Electronics Letters*, vol. 31, pp. 497-498, 1995, and references therein.

[13] A. Jaksic, G. Ristic, M. Pejovic, A. Mohammadzadeh, C. Sudre, and W. Lane, "Gamma-Ray Irradiation and Post-Irradiation Response of Low Sensitivity/High Dose Range RADFETs", in *Proc. RADECS 2001 Conference*, Grenoble, France, 2001, in press.

[14] R.K. Freitag, D.B. Brown, and C.M. Dozier, "Experimental Evidence of Two Species of Radiation Induced Trapped Positive Charge", *IEEE Trans. Nucl. Sci*., vol. 40, pp. 1316-1322, 1993, and references therein.

.

Report on PSI Irradiation Campaign in June 2001

Confidentiality Status: **Commercial-in-confidence**

Prepared for: **Ali Mohammadzadeh, ESA-ESTEC**

Prepared by: **Aleksandar Jaksic**

Date: **January 31, 2002**

Devices & Systems for Dosimetry, Transducers Group
National Microelectronics Research Centre (NMRC)
University College Cork, Lee Maltings, Prospect Row, Cork, Ireland
http://www.nmrc.ie/projects/radfets/index.html
Tel.: +353 21 490 4262
Fax: +353 21 427 0271
Email: ajaksic@nmrc.ie

Contents

Introduction

This report presents relevant information related to the proton irradiation campaign that took place at PSI from 26-30 June 2001, under the 2000/2001 MTSL RADFET Dosimeter Development and Supply Programme. Direct participants in the campaign were Aleksandar Jaksic (NMRC) and Wojtek Hajdas (PSI). After the intriguing initial proton irradiation results from 1999 [1,2], this new campaign was designed to investigate in more detail various aspects of the NMRC RADFETs proton response. These aspects include correlation with existing Co-60 data, proton energy dependence, and the effects of device type, geometry, irradiation bias and package lids.

The organisation of the report is as follows. Experimental details are described in the next section. The following section gives the experimental results, and the last section contains discussion of results and conclusions relevant for the future work.

Experimental details

Table 1 gives an overview of the RADFET samples used in the experiment.

Table 1: Experimental samples – an overview.

Type	Mask-set	Lot No.	Date code	Quantity
400nm IMPL	ESAPMOS4 (E4)	P1152-W2	MIL 2400	18
400nm IMPL	ESAPMOS2 (E2)	P210-W6	MIL 0021	12
400nm UNIMPL	"	P172-W5	STD 9851	6
100nm UNIMPL	"	P129-W4	MIL 9928	2

The ESAPMOS4 (E4) RADFET chip contains four RADFETs, as follows [3]: 300/50 with all four terminals accessible[1] (RADFET1), 690/15 with all four terminals accessible (RADFET2), 300/50 with two terminals accessible[2] (RADFET3), and 690/15 with two terminals accessible (RADFET4). All four RADFETs were monitored during experiments. The ESAPMOS2 (E2) RADFET chip contains two RADFETs: 300/50 and 868/11; only 300/50 RADFETs were monitored during experiment. All devices were packaged in standard ceramic 14-pin DIL packages. Some E4 samples were irradiated with standard kovar package lids and some without lids. All E2 samples were irradiated with kovar lids.

The RADFETs were irradiated with protons at the energies of 10.4, 60.1 and 300 MeV[3]. The LET values corresponding to these energies are 77.95, 19.92 and 6.66 MeV/cm, respectively. Protons with the first two energies were delivered in the PSI OPTIS area, while 300 MeV proton irradiation was performed in the PIF area. During irradiations, proton beams were often unstable (occasionally would even shut down), with different intensities/dose rates. Irradiation at each proton energy consisted of two runs. The first run involved E4 samples, and the second run E2 ones. The RADFETs were placed in the area 3cm in diameter. As advised by the PSI, beam non-uniformities in this area were within 5% (reference point: centre of the beam). The maximum absorbed dose (D_{max}) was 30 krad for all runs except the second run at 300 MeV. This run was completed at the maximum dose of 10 krad because of frequent problems with the proton beam. During irradiation, B, S, and D terminals were always grounded, while irradiation bias (V_{IRR}) of 0V or +5V was applied at the G. Table 2 summarises relevant irradiation parameters.

Table 2: Summary of relevant irradiation parameters.

Run	Energy	Mask-set	Dose rate	Measurement points (krad)
1.1	10 MeV	E4	Unstable, 7-40 rad/s	0.5, 1, 5, 10, 20, 30
1.2	"	E2	Rather stable, 40 rad/s	"
2.1	60 MeV	E4	Stable, 15 rad/s	"
2.2	"	E2	Unstable, 10-15 rad/s	"
3.1	300 MeV	E4	Rather stable, 4 rad/s	"
3.2	"	E2	Unstable, frequent beam shut-downs	0.5, 1, 5, 10

[1] Four terminals: Bulk (B), Source (S), Gate (G) and Drain (D).

[2] Accessible terminals: B=S and D=G.

[3] These are the exact mean energies of the proton beams at the location of the RADFET samples. In further text, these energies will be referred to as 10, 60 and 300 MeV.

The aim of experiment was providing initial calibration data for proton environment and investigation of the following aspects of proton response:

- correlation with existing Co-60 data,
- proton energy dependence (for 10 MeV, 60 MeV, and 300 MeV protons),
- effects of device type (400nm IMPL, 400nm UNIMPL, 100nm UNIMPL),
- effects of mask-set revision (E4 vs. E2 mask-set for 400nm IMPL),
- effects of device geometry (300/50 vs. 690/15 E4 RADFETs),
- effects of irradiation bias (V_{IRR}=0V vs. V_{IRR}=+5V),
- effects of package lids (kovar lids attached to or removed from standard ceramic 14-pin DIL packages; lid effects were investigated only for E4 samples).

Table 3 summarises irradiation conditions for all experimental samples. It should be noted that the bias conditions for E4 chips given in Table 3 are valid only for RADFET1 and RADFET2. As RADFET3 and RADFET4 have G and D internally connected, and it is advisable that B, S and D be at the same potential during irradiation, these RADFETs were always irradiated with all terminals grounded.

Table 3: Irradiation conditions for experimental samples.

Energy / Run	**Type (mask-set)**	Label	V_{IRR}(V)	Lid
10 MeV / 1.1	400nm IMPL (E4)	I-076	0	Yes
"	"	I-078	0	No
"	"	I-053	+5	Yes
"	"	I-054	+5	Yes
"	"	I-055	+5	No
"	"	I-057	+5	No
10 MeV / 1.2	400nm IMPL (E2)	I-012	0	Yes
"	"	I-033	0	Yes
"	"	I-044	+5	Yes
"	"	I-052	+5	Yes
"	400nm UNIMPL (E2)	U-181	0	Yes
"	"	U-188	+5	Yes
60 MeV / 2.1	400nm IMPL (E4)	I-073	0	Yes
"	"	I-075	0	No
"	"	I-056	+5	Yes
"	"	I-058	+5	Yes
"	"	I-064	+5	No
"	"	I-059	+5	No
60 MeV / 2.2	400nm IMPL (E2)	I-061	0	Yes
"	"	I-063	0	Yes
"	"	I-074	+5	Yes
"	"	I-156	+5	Yes
"	400nm UNIMPL (E2)	U-190	0	Yes
"	"	U-195	+5	Yes
300 MeV / 3.1	400nm IMPL (E4)	I-069	0	Yes
"	"	I-074	0	No
"	"	I-071	+5	Yes
"	"	I-060	+5	Yes
"	"	I-072	+5	No
"	"	I-067	+5	No
300 MeV / 3.2	400nm IMPL (E2)	I-159	0	Yes
"	"	I-177	0	Yes
"	"	I-190	+5	Yes
"	"	I-194	+5	Yes
"	400nm UNIMPL (E2)	U-196	0	Yes
"	"	U-238	+5	Yes
"	100nm UNIMPL (E2)	S-045	0	Yes
"	"	S-049	+5	Yes

Electrical measurements were done in a remote mode, i.e. the irradiation was interrupted, samples measured off the radiation site, and then returned to the site for the next irradiation step. The total time needed to switch the proton beam off, enter the radiation site, take the samples, mount the samples again and switch the beam on was approx. 15 minutes in all cases. Electrical measurements lasted approx. 30 minutes in the irradiation runs related to E4 devices (runs 1.1, 2.1 and 3.1), and 10 minutes in the runs related to E2 devices (runs 1.2, 2.2 and 3.2). Thus, the total time between switching the beam off and switching it on again was 45 minutes (E4 runs) and 25 minutes (E2 runs). Electrical measurements consisted of the threshold voltage (V_T) measurements in the so called Reader Circuit configuration, shown in Fig. 1. The Icurr value of 10µA was supplied and the voltage (V_O=V_{th}=V_T) measured by the Keithley 237 Source Measure Unit.

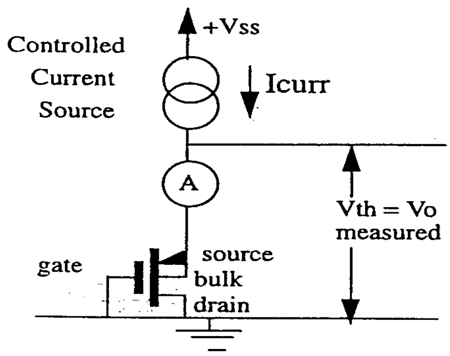

Figure 1: Reader Circuit configuration used for threshold voltage (V_T) measurements; Icurr=10µA.

Experimental results

Tables

Tables 4-9 show measured threshold voltage shifts (ΔV_T) during different irradiation runs.

Table 4: Threshold voltage shifts for the ESAPMOS4 samples irradiated in Run 1.1.

Date: 26/06/01; Proton energy: 10.4 MeV; LET: 77.95 MeV/cm; Dose rate: unstable (7-10, 15-18, often 30-40 rad/s)
Samples: 400nm IMPL, P1152-W2 (ESAPMOS4)
Samples irradiated with package lids are in red, samples irradiated without package lids are in blue.

$V_{IRR} = 0V$

D(rad)	I-076/1	I-076/2	I-076/3	I-076/4	I-078/1	I-078/2	I-078/3	I-078/4
500	0.1533	0.1552	0.1518	0.1621	0.1742	0.1573	0.1770	0.1798
1000	0.3165	0.3119	0.3156	0.3228	0.3500	0.3156	0.3557	0.3447
5000	1.4666	1.3585	1.4105	1.4072	1.3780	1.1775	1.3795	1.2772
10000	2.4161	2.2857	2.3382	2.2978	2.2684	1.8896	2.2669	2.0703
20000	3.7874	3.5627	3.6822	3.5621	3.5366	2.7560	3.5880	3.1650
30000	4.8180	4.4338	4.7392	4.5137	4.4288	3.2908	4.5756	3.9018

$V_{IRR} = +5V$

D(rad)	I-053/1	I-053/2	I-053/3	I-053/4	I-054/1	I-054/2	I-054/3	I-054/4
500	0.4862	0.4166	0.1974	0.1950	0.4409	0.3700	0.1806	0.1526
1000	0.9117	0.8261	0.3920	0.3816	0.8577	0.7664	0.3672	0.3337
5000	3.8804	3.6612	1.4678	1.4529	4.1586	3.9215	1.5625	1.5242
10000	7.0613	6.7091	2.3914	2.3474	7.4162	7.0503	2.5099	2.4457
20000	12.342	11.918	3.8634	3.7484	12.555	12.083	3.9608	3.8220
30000	16.372	15.887	4.9720	4.7245	16.677	16.247	5.7113	4.9140

D(rad)	I-055/1	I-055/2	I-055/3	I-055/4	I-057/1	I-057/2	I-057/3	I-057/4
500	0.3371	0.2915	0.1630	0.1549	0.3689	0.2602	0.1762	0.1190
1000	0.6377	0.5630	0.3125	0.2964	0.6909	0.5563	0.3415	0.2698
5000	2.8198	2.5399	1.2220	1.1378	3.1513	2.8341	1.3664	1.2216
10000	5.1742	4.6557	2.0063	1.8451	5.5489	5.0072	2.1476	1.9252
20000	10.222	9.2548	3.4510	3.0687	10.187	9.3401	3.4095	2.9956
30000	13.825	12.747	4.4791	3.8409	13.799	12.998	4.3320	3.6752

Table 5: Threshold voltage shifts for the ESAPMOS2 samples irradiated in Run 1.2.

Date: 26/06/01; Proton energy: 10.4 MeV; LET: 77.95 MeV/cm; Dose rate: unstable (30-40 rad/s)
Samples: 400nm IMPL, P210-W6 (ESAPMOS2) and 400nm UNIMPL, P172-W5 (ESAPMOS2)
All samples irradiated with package lids. Samples irradiated with V_{IRR}=0V are in red, samples irradiated V_{IRR}=+5V in blue.

D(rad)	I-012	I-033	I-044	I-052	U-181	U-188
500	0.1620	0.1501	0.3599	0.3847	0.0260	0.0460
1000	0.3031	0.2810	0.6858	0.7312	0.0550	0.0970
5000	1.1429	1.0739	3.2609	3.4723	0.2810	0.6000
10000	1.8701	1.7904	6.3440	6.7850	0.4890	1.2290
20000	2.9918	2.8173	11.193	11.858	0.8350	2.2200
30000	3.9016	3.7646	15.497	16.509	1.2010	3.1780

Table 6: Threshold voltage shifts for the ESAPMOS4 samples irradiated in Run 2.1.

Date: 27/06/01; Proton energy: 60.1 MeV; LET: 19.92 MeV/cm; Dose rate: rather stable (~15 rad/s)
Samples: 400nm IMPL, P1152-W2 (ESAPMOS4)
Samples irradiated with package lids are in red, samples irradiated without package lids are in blue.

$V_{IRR} = 0V$

D(rad)	I-073/1	I-073/2	I-073/3	I-073/4	I-075/1	I-075/2	I-075/3	I-075/4
500	0.8082	0.7966	0.8157	0.7818	0.7247	failed	0.7384	0.6740
1000	1.3562	1.2942	1.3431	1.3000	1.2105	-	1.2183	1.1320
5000	4.0944	3.8630	4.0341	3.8658	3.6896	-	3.7663	3.2899
10000	6.0734	5.5777	6.0513	5.6160	5.3264	-	5.6104	4.6183
20000	8.3694	7.5376	8.4313	7.6913	7.4215	-	7.8264	6.2688
30000	9.9244	8.7686	10.143	9.0713	8.9965	-	9.4824	7.6238

$V_{IRR} = +5V$

D(rad)	I-056/1	I-056/2	I-056/3	I-056/4	I-058/1	I-058/2	I-058/3	I-058/4
500	1.6024	1.5474	0.7645	0.7328	1.3760	1.2915	0.6748	0.6112
1000	2.8230	2.7368	1.2785	1.2356	2.5554	2.4321	1.2167	1.1385
5000	12.335	12.036	3.7089	3.5698	11.042	10.811	4.0337	3.3654
10000	21.083	20.803	5.7504	5.3937	19.013	18.797	6.5200	5.1564
20000	33.265	32.866	8.1424	7.4937	30.161	29.995	8.5450	7.3090
30000	40.077	39.870	9.5014	8.6217	37.316	37.378	10.756	8.5290

D(rad)	I-064/1	I-064/2	I-064/3	I-064/4	I-059/1	I-059/2	I-059/3	I-059/4
500	1.0172	0.8646	0.5239	0.4774	0.9678	0.8441	0.5021	0.4419
1000	2.0146	1.7470	1.0013	0.9124	2.1003	1.8439	1.0393	0.9433
5000	7.5953	6.8040	2.6819	2.3735	6.8708	6.2252	2.5135	2.2356
10000	14.288	13.308	4.2776	3.6354	13.562	12.749	4.1067	3.5084
20000	23.864	22.926	6.3459	5.1110	22.727	22.024	6.0861	4.9102
30000	28.401	27.778	7.3419	5.8567	25.980	25.683	6.8531	5.4770

Table 7: Threshold voltage shifts for the ESAPMOS2 samples irradiated in Run 2.2.

Date: 27/06/01; Proton energy: 60.1 MeV; LET: 19.92 MeV/cm; Dose rate: rather unstable (10-15 rad/s)
Samples: 400nm IMPL, P210-W6 (ESAPMOS2) and 400nm UNIMPL, P172-W5 (ESAPMOS2)
All samples irradiated with package lids. Samples irradiated with V_{IRR}=0V are in red, samples irradiated V_{IRR}=+5V in blue.

D(rad)	I-061	I-063	I-074	I-156	U-190	U-195
500	0.6853	0.5691	1.6031	1.1683	0.1100	0.1070
1000	1.1790	1.0033	3.0171	2.2145	0.1830	0.2140
5000	3.1894	2.6310	11.722	8.1175	0.4710	0.6270
10000	4.9733	4.1676	20.032	15.076	0.8050	1.3810
20000	7.5223	6.3122	30.316	23.318	1.2450	2.1740
30000	9.4673	8.0902	37.624	30.641	1.7290	3.3860

Table 8: Threshold voltage shifts for the ESAPMOS4 samples irradiated in Run 3.1.

Date: 30/06/01; Proton energy: 300 MeV; LET: 6.66 MeV/cm; Dose rate: rather stable (~4 rad/s)
Samples: 400nm IMPL, P1152-W2 (ESAPMOS4)
Samples irradiated with package lids are in red, samples irradiated without package lids are in blue.

$V_{IRR} = 0V$

D(rad)	I-069/1	I-069/2	I-069/3	I-069/4	I-074/1	I-074/2	I-074/3	I-074/4
500	0.4329	0.3950	0.4333	0.3945	0.2939	0.2749	0.2886	0.2613
1000	0.8235	0.7554	0.8281	0.7814	0.5551	0.5282	0.5480	0.5125
5000	2.7650	2.5668	2.7425	2.5942	1.8876	1.7515	1.8385	1.7544
10000	4.4393	4.1274	4.3776	4.1172	2.7348	2.5358	2.6840	2.5553
20000	6.6930	6.0333	6.7008	6.1195	3.7859	3.4748	3.7709	3.5399
30000	7.8080	6.9626	7.9538	7.1810	4.5077	4.1075	4.5386	4.2154

$V_{IRR} = +5V$

D(rad)	I-071/1	I-071/2	I-071/3	I-071/4	I-060/1	I-060/2	I-060/3	I-060/4
500	0.8121	0.7526	0.4423	0.4220	0.7939	0.7184	0.4340	0.3382
1000	1.5827	1.5034	0.8418	0.8103	1.5449	1.4622	0.8261	0.7271
5000	6.8916	6.6471	2.7942	2.6441	6.6894	6.4747	2.8175	2.5224
10000	12.096	11.808	4.4576	4.2146	11.676	11.429	4.5712	3.9273
20000	19.653	19.421	6.8809	6.3191	18.950	18.871	6.8133	5.5517
30000	24.937	24.868	8.2039	7.4091	24.204	24.267	7.9983	6.4690

D(rad)	I-072/1	I-072/2	I-072/3	I-072/4	I-067/1	I-067/2	I-067/3	I-067/4
500	0.6465	0.5494	0.3752	0.2969	0.6480	0.5281	0.3754	0.2448
1000	1.2602	1.0896	0.7115	0.5982	1.2658	1.0643	0.7159	0.5481
5000	5.4927	5.0093	2.3054	1.9390	5.4882	4.9686	2.3224	1.9085
10000	9.6237	9.0798	3.5534	2.7962	9.6362	9.0067	3.5556	2.7594
20000	16.112	15.845	5.0923	3.8465	16.131	15.690	5.1186	3.7876
30000	20.950	20.900	6.0594	4.5652	20.943	20.682	6.0578	4.4921

Table 9: Threshold voltage shifts for the ESAPMOS2 samples irradiated in Run 3.2.

Date: 30/06/01; Proton energy: 300 MeV; LET: 6.66 MeV/cm; Dose rate: unstable, frequent beam shut downs
Samples: 400nm IMPL, P210-W6; 400nm UNIMPL, P172-W5; and 100nm UNIMPL, P129-W4 (all ESAPMOS2)
All samples irradiated with package lids. Samples irradiated with V_{IRR}=0V are in red, samples irradiated V_{IRR}=+5V in blue.

D(rad)	I-159	I-177	I-190	I-194	U-196	U-238	S-045	S-049
500	0.3054	0.2885	0.6305	0.6587	0.0920	0.1120	0.0113	0.0412
1000	0.5813	0.5410	1.2225	1.2688	0.1610	0.2150	0.0176	0.0925
5000	1.8792	1.6996	5.2501	5.3887	0.4860	0.9570	0.1211	0.4407
10000	2.9867	2.6916	9.5401	9.7617	0.8120	1.7860	0.2161	0.8359

To enable comparison with Co-60 RADFET response, the calibration curves in Table 10, based on previous ESTEC Co-60 data for E2 devices, were used.

Table 10: Calibration curves for Co-60 irradiation for three different RADFET types used in PSI proton experiment (D in rads, ΔV_T in Volts).

V_{IRR}/Type	400nm IMPL	400nm UNIMPL	100nm UNIMPL
V_{IRR}=0V	$\Delta V_T=0.0041D^{0.6987}$	$\Delta V_T=0.0007D^{0.7719}$	$\Delta V_T=0.00005D^{0.8928}$
V_{IRR}=+5V	$\Delta V_T=0.0049D^{0.8137}$	$\Delta V_T=0.0006D^{0.8569}$	$\Delta V_T=0.0002D^{0.9126}$

Based on calibration curves in Table 10, the estimated ΔV_T values for Co-60 for relevant doses were calculated and are shown in Table 11. These Co-60 data will be compared with proton data obtained during the PSI experiment. There are still no Co-60 data in the dose range in question for E4 400nm IMPL RADFET, hence equivalent E2 Co-60 data will be used for comparison with both E2 and E4 PSI proton data.

Table 11: Estimated threshold voltage shifts for Co-60 irradiation for device types and doses relevant for PSI experiment.

Type Þ	400nm IMPL		400nm UNIMPL		100nm UNIMPL	
D (rad) ß	V_{IRR}=0V	V_{IRR}=+5V	V_{IRR}=0V	V_{IRR}=+5V	V_{IRR}=0V	V_{IRR}=+5V
500	0.3152	0.7697	0.0848	0.1438	0.0128	0.0581
1000	0.5116	1.3530	0.1448	0.2233	0.0238	0.1094
5000	1.5749	5.0124	0.5016	1.0345	0.1003	0.4750
10000	2.5561	8.8104	0.8564	1.8737	0.1863	0.8942
20000	4.1487	15.4862	1.4624	3.3935	-	-
30000	5.5080	21.5392	1.9998	4.8033	-	-

Based on Table 3 and taking into account experimental details for all four RADFETs on the E4 chip, the total of 38 sample groups can be distinguished in the PSI experiment: 24 related to E4 chip and 12 related to E2 chip. These sample groups are described in Table 12. Number of samples in sample groups ranges from 1 to 4. Table 12 also shows ΔV_T data during irradiation for all sample groups, i.e. mean ΔV_T values and standard deviations for the groups with 4 samples, and only mean ΔV_T values for the groups of 2 samples. These mean values and standard deviations (if applicable) are shown in the figures in the next section.

Table 12: Description of sample groups for the PSI irradiation experiments and statistically processed ΔV_T data during irradiation. Mean ΔV_T[V] is given for all sample groups and, in addition, standard deviation is given (in blue) for sample groups with 4 samples.

ESAPMOS4 RADFETs							Dose (rad)					
Gr no	**Geom (type)[4]**	**E [MeV]**	**V_{IRR} [V]**	**Lid**	**No. of sampl.**	**Samples list**	500	1000	5000	10000	20000	30000
1	300/50	10	0	yes	4	I-076/1, I-076/3	0.17077	0.34783	1.47685	2.41390	3.82345	5.06012
						I-053/3, I-054/3	0.02214	0.03806	0.06305	0.07178	0.11792	0.44475
2	690/15	10	0	yes	4	I-076/2, I-076/4	0.16623	0.33750	1.43570	2.34415	3.67380	4.64650
						I-053/4, I-054/4	0.01960	0.03072	0.07048	0.07277	0.13210	0.21642
3	300/50	10	0	no	4	I-078/1, I-078/3	0.17260	0.33993	1.33648	2.17230	3.49627	4.45388
						I-055/3, I-057/3	0.00651	0.01919	0.07654	0.12430	0.08087	0.10155
4	690/15	10	0	no	4	I-078/2, I-078/4	0.15275	0.30662	1.20353	1.93255	2.99632	3.67718
						I-055/4, I-057/4	0.02514	0.03157	0.05987	0.09750	0.17459	0.27480
5	300/50	60	0	yes	4	I-073/1, I-073/3	0.76580	1.29862	3.96777	6.09877	8.37203	10.0812
						I-056/3, I-058/3	0.06473	0.06432	0.17492	0.31712	0.16948	0.52279
6	690/15	60	0	yes	4	I-073/2, I-073/4	0.73060	1.24207	3.66600	5.43595	7.50790	8.74765
						I-056/4, I-058/4	0.08414	0.07493	0.24382	0.21011	0.15735	0.23725
7	300/50	60	0	no	4	I-075/1, I-075/3	0.62227	1.11735	3.16283	4.83028	6.91998	8.16847
						I-064/3, I-059/3	0.12662	0.11318	0.65691	0.74917	0.83627	1.26826
8	690/15	60	0	no	3 of 4[5]	I-075/2, I-075/4	0.53110	0.99590	2.63300	3.92070	5.43000	6.31917
						I-064/4, I-059/4	0.12502	0.11887	0.57306	0.60747	0.73333	1.14569
9	300/50	300	0	yes	4	I-069/1, I-069/3	0.43562	0.82987	2.77980	4.46143	6.77200	7.99100
						I-071/3, I-060/3	0.00447	0.00817	0.03286	0.08079	0.09106	0.16356
10	690/15	300	0	yes	4	I-069/2, I-069/4	0.38743	0.76855	2.58188	4.09662	6.00590	7.00542
						I-071/4, I-060/4	0.03524	0.03559	0.05095	0.12105	0.32560	0.40140
11	300/50	300	0	no	4	I-074/1, I-074/3	0.33327	0.63262	2.08847	3.13195	4.44193	5.29087
						I-072/3, I-067/3	0.04857	0.09368	0.26116	0.48836	0.76627	0.88658
12	690/15	300	0	no	4	I-074/2, I-074/4	0.26947	0.54675	1.83835	2.66167	3.66220	4.34505
						I-072/4, I-067/4	0.02204	0.03727	0.09940	0.13516	0.18236	0.21858
13	300/50	10	+5	yes	2	I-053/1, I-054/1	0.46355	0.88470	4.01950	7.23875	12.4485	16.5245
14	690/15	10	+5	yes	2	I-053/2, I-054/2	0.39330	0.79625	3.79135	6.87970	12.0005	16.0670
15	300/50	10	+5	no	2	I-055/1, I-057/1	0.35300	0.66430	2.98555	5.36155	10.2045	13.8120
16	690/15	10	+5	no	2	I-055/2, I-057/2	0.27585	0.55965	2.68700	4.83145	9.29745	12.8725
17	300/50	60	+5	yes	2	I-056/1, I-058/1	1.48920	2.68920	11.6885	20.0480	31.7130	38.6965
18	690/15	60	+5	yes	2	I-056/2, I-058/2	1.41945	2.58445	11.4235	19.8000	31.4305	38.6240
19	300/50	60	+5	no	2	I-064/1, I-059/1	0.99250	2.05745	7.23305	13.9250	23.2955	27.1905
20	690/15	60	+5	no	2	I-064/2, I-059/2	0.85435	1.79545	6.51460	13.0285	22.4750	26.7305
21	300/50	300	+5	yes	2	I-071/1, I-060/1	0.80300	1.56380	6.79050	11.8860	19.3015	24.5705
22	690/15	300	+5	yes	2	I-071/2, I-060/2	0.73550	1.48280	6.56090	11.6185	19.1460	24.5675
23	300/50	300	+5	no	2	I-072/1, I-067/1	0.64725	1.26300	5.49045	9.62995	16.1215	20.9465
24	690/15	300	+5	no	2	I-072/2, I-067/2	0.53875	1.07695	4.98895	9.04325	15.7675	20.7910
ESAPMOS2 RADFETs												
25	400 I	10	0	yes	2	I-012, I-033	0.15605	0.29205	1.10840	1.83025	2.90455	3.83310
26	400 I	10	+5	yes	2	I-044, I-052	0.37230	0.70850	3.36660	6.56450	11.5255	16.0030
27	400 U	10	0	yes	1	U-181	0.026	0.055	0.281	0.489	0.835	1.201
28	400 U	10	+5	yes	1	U-188	0.046	0.097	0.600	1.229	2.22	3.178
29	400 I	60	0	yes	2	I-061, I-063	0.62720	1.09115	2.91020	4.57045	6.91725	8.77875
30	400 I	60	+5	yes	2	I-074, I-156	1.38570	2.61580	9.91975	17.5540	26.8170	34.1325
31	400 U	60	0	yes	1	U-190	0.110	0.183	0.471	0.805	1.245	1.729
32	400 U	60	+5	yes	1	U-195	0.107	0.214	0.627	1.381	2.174	3.386
33	400 I	300	0	yes	2	I-159, I-177	0.29695	0.56115	1.78940	2.83915	-	-
34	400 I	300	+5	yes	2	I-190, I-194	0.64460	1.24565	5.31940	9.65090	-	-
35	400 U	300	0	yes	1	U-196	0.092	0.161	0.486	0.812	-	-
36	400 U	300	+5	yes	1	U-238	0.112	0.215	0.957	1.786	-	-
37	100 U	300	0	yes	1	S-045	0.01130	0.01760	0.12110	0.21610	-	-
38	100 U	300	+5	yes	1	S-049	0.04120	0.09250	0.44070	0.83590	-	-

[4] Geometry (W/L, both in µm) for E4 samples, device type always 400nm IMPL; device type for E2 samples (gate oxide thickness [nm] followed by I for implanted, or U for unimplanted gate oxide devices), geometry always 300/50.

[5] Sample I-075/2 failed at the beginning of the irradiation run.

Figures

Figures 1 – 27 summarise the main experimental results. Data in the figures are taken from Table 11 (Co-60 data) and Table 12 (proton data).

Figures 2 – 14 show ΔV_T for various 300/50 samples (both E2 and E4) for three different proton energies.

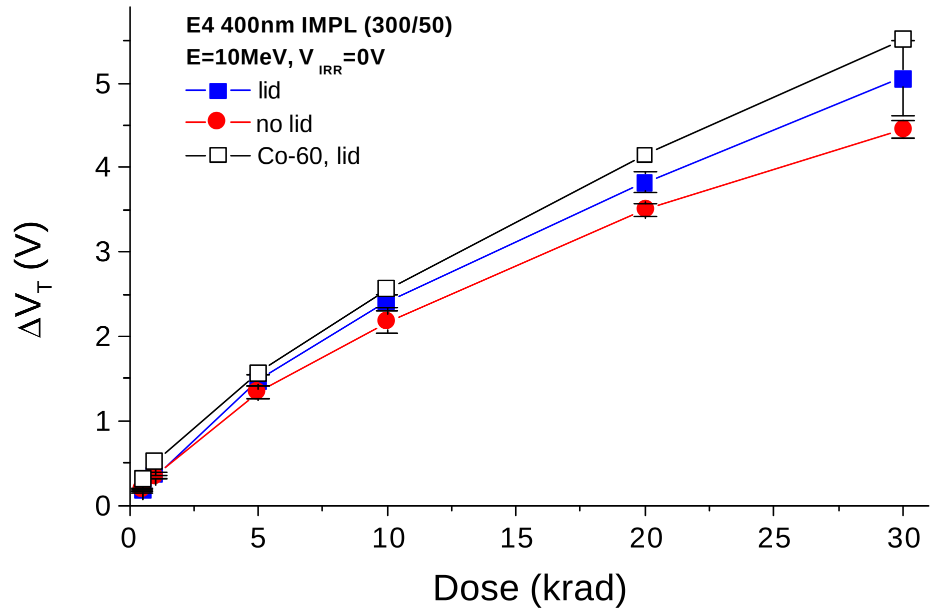

Figure 2: ΔV_T for 300/50 E4 400nm IMPL samples for proton (E=10MeV) and Co-60 irradiations; V_{IRR}=0V.

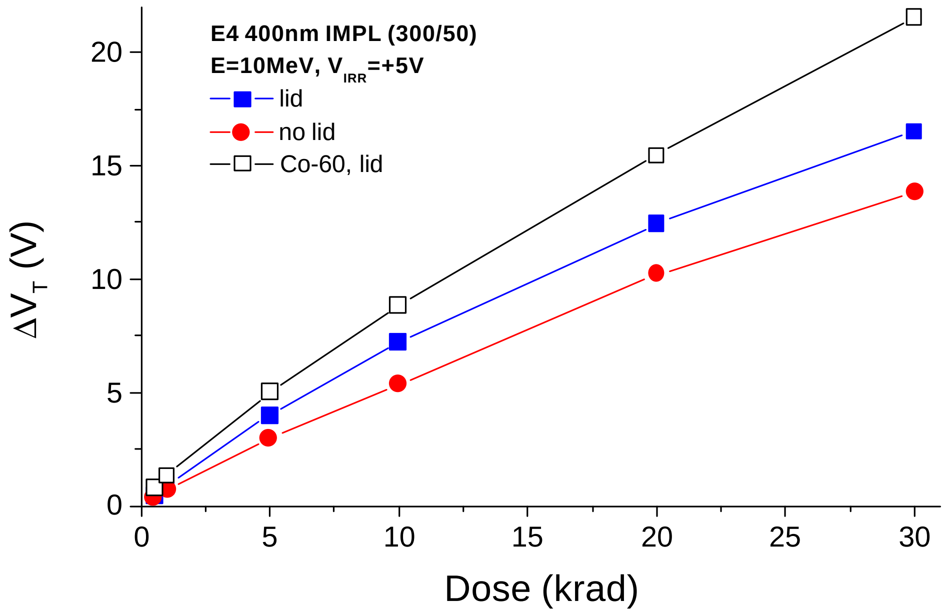

Figure 3: ΔV_T for 300/50 E4 400nm IMPL samples for proton (E=10MeV) and Co-60 irradiations; V_{IRR}=+5V.

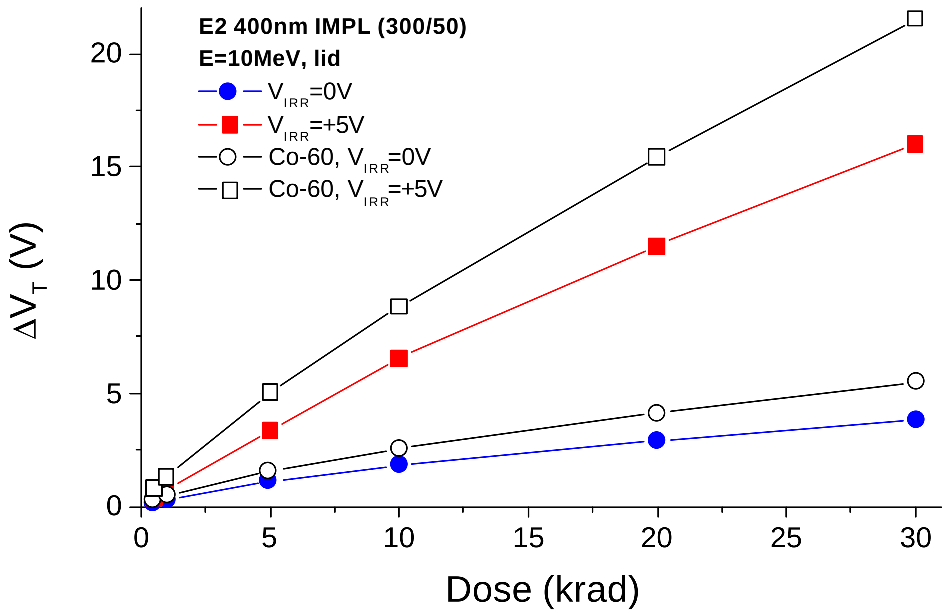

Figure 4: ΔV_T for 300/50 E2 400nm IMPL samples for proton (E=10MeV) and Co-60 irradiations.

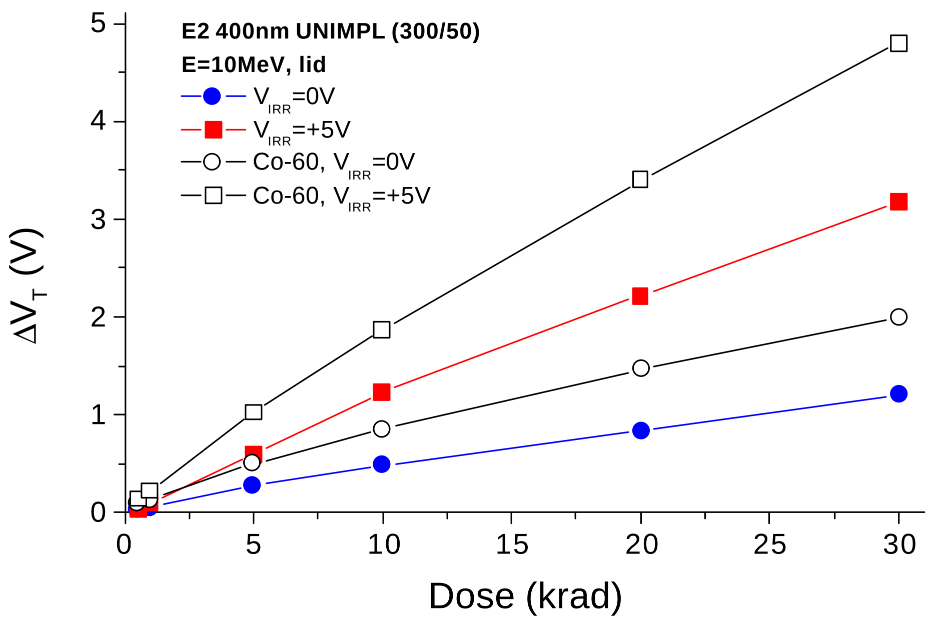

Figure 5: ΔV_T for 300/50 E2 400nm UNIMPL samples for proton (E=10MeV) and Co-60 irradiations.

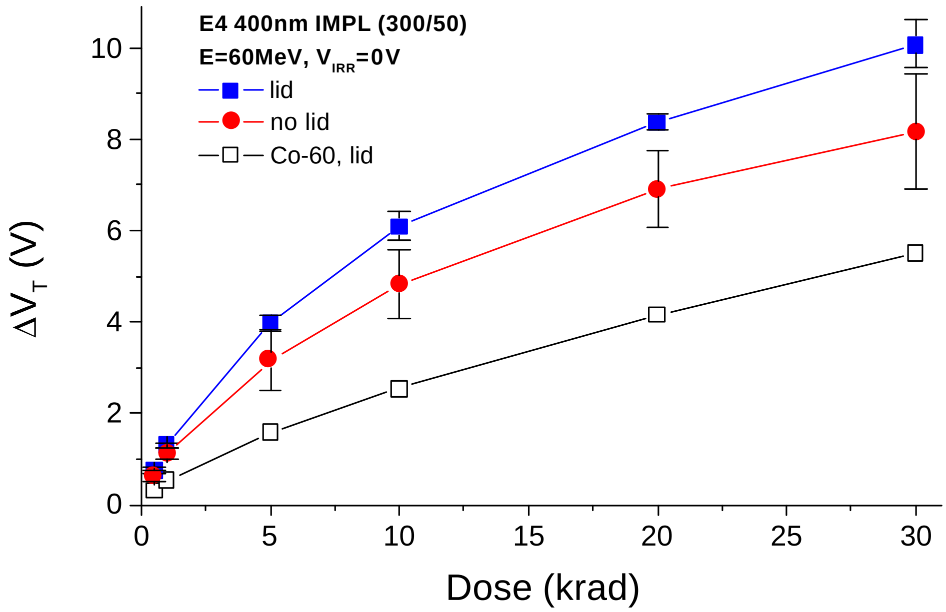

Figure 6: ΔV_T for 300/50 E4 400nm IMPL samples for proton (E=60MeV) and Co-60 irradiations; V_{IRR}=0V.

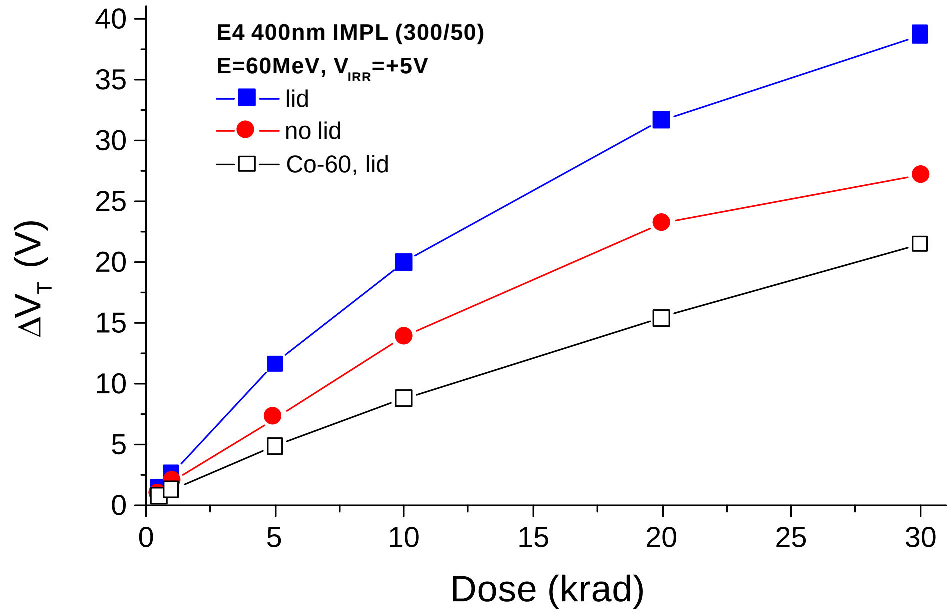

Figure 7: ΔV_T for 300/50 E4 400nm IMPL samples for proton (E=60MeV) and Co-60 irradiations; V_{IRR}=+5V.

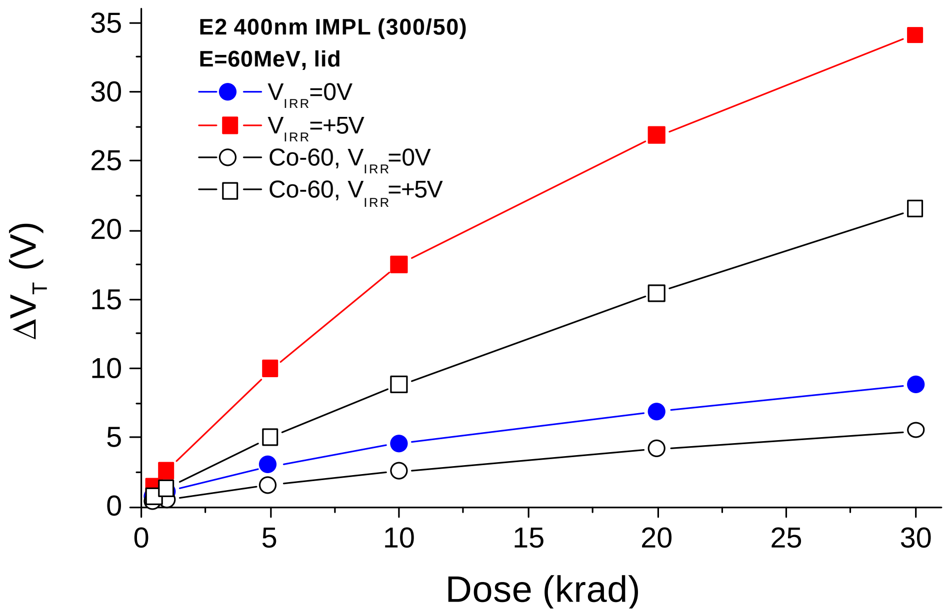

Figure 8: ΔV_T for 300/50 E2 400nm IMPL samples for proton (E=60MeV) and Co-60 irradiations.

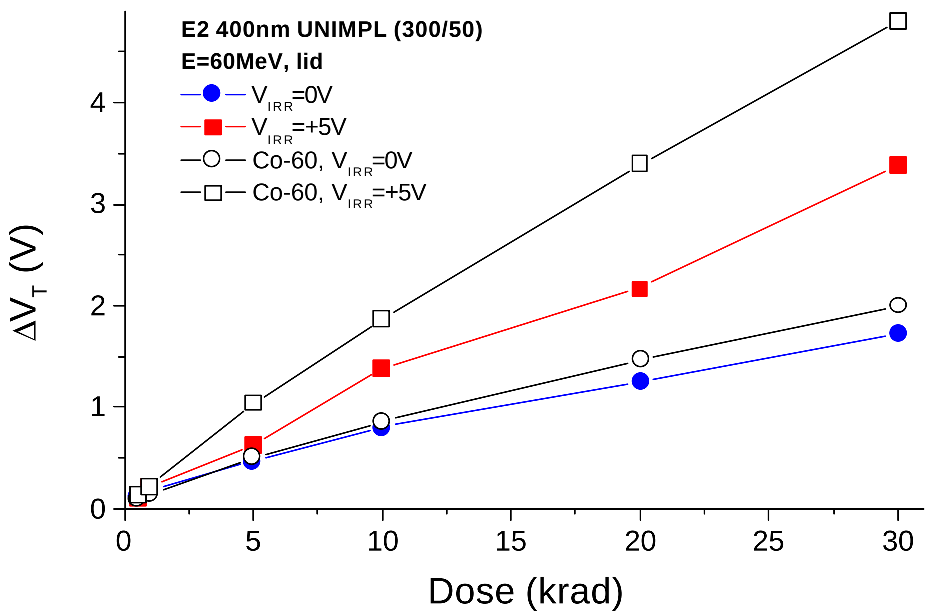

Figure 9: ΔV_T for 300/50 E2 400nm UNIMPL samples for proton (E=60MeV) and Co-60 irradiations.

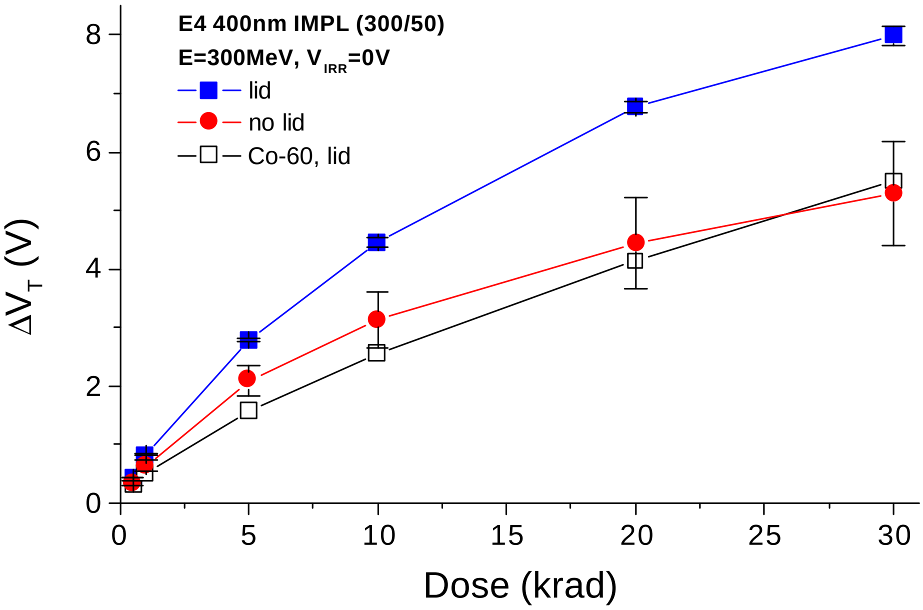

Figure 10: ΔV_T for 300/50 E4 400nm IMPL samples for proton (E=300MeV) and Co-60 irradiations; V_{IRR}=0V.

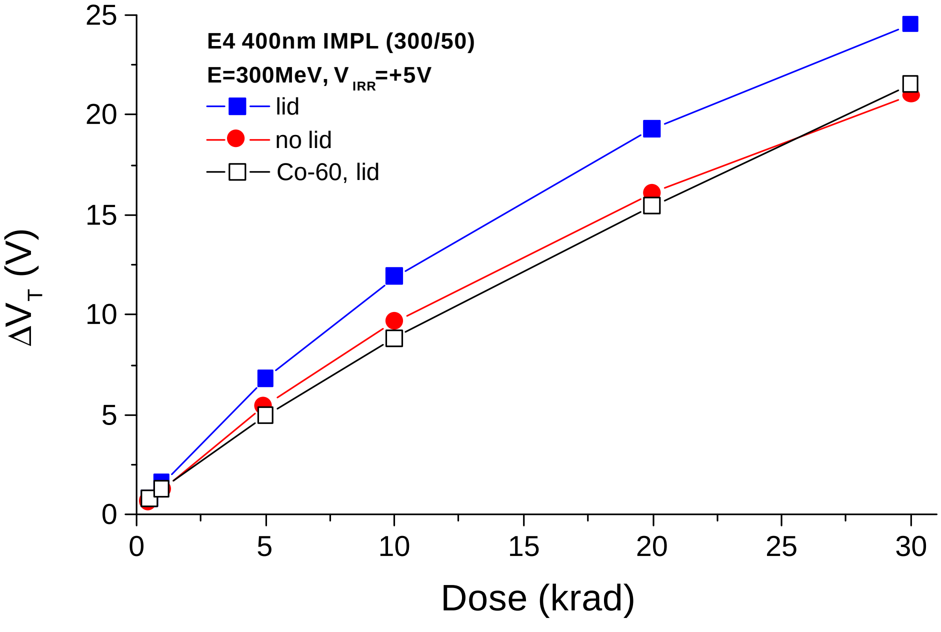

Figure 11: ΔV_T for 300/50 E4 400nm IMPL samples for proton (E=300MeV) and Co-60 irradiations; V_{IRR}=+5V.

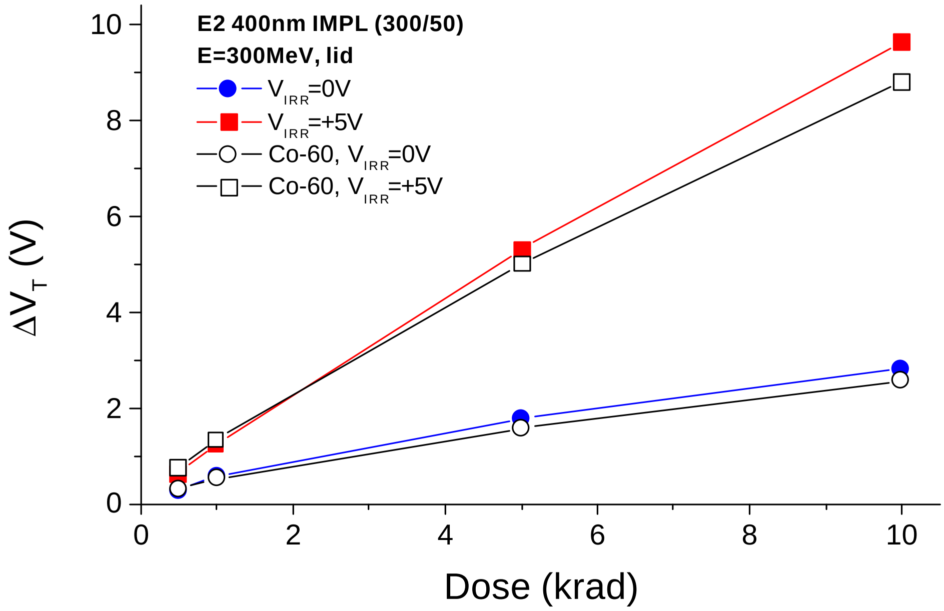

Figure 12: ΔV_T for 300/50 E2 400nm IMPL samples for proton (E=300MeV) and Co-60 irradiations.

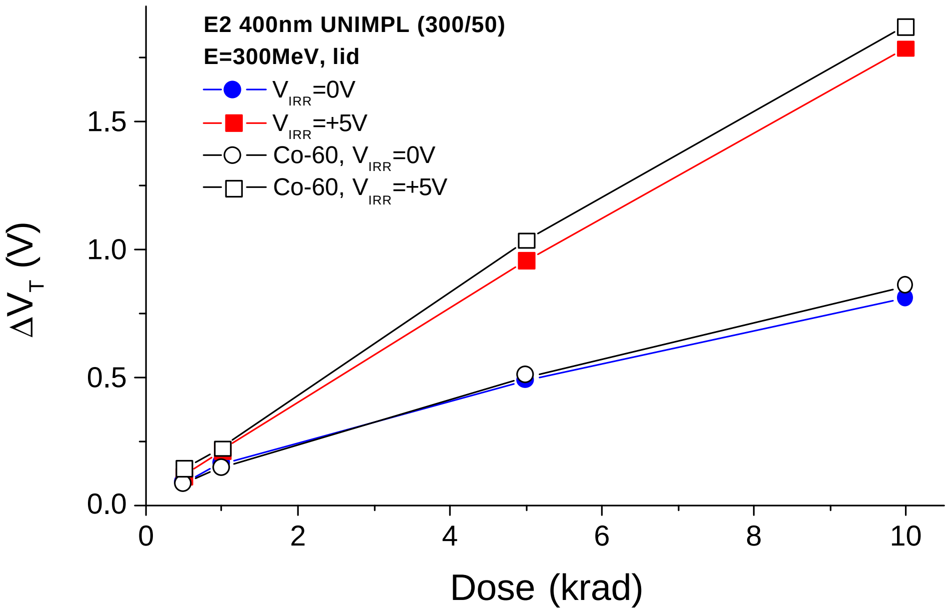

Figure 13: ΔV_T for 300/50 E2 400nm UNIMPL samples for proton (E=300MeV) and Co-60 irradiations.

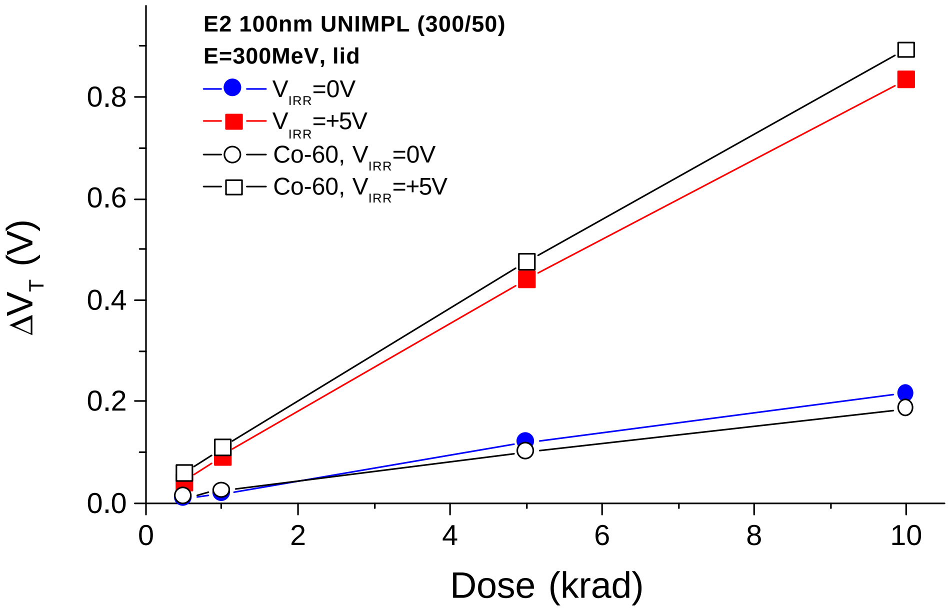

Figure 14: ΔV_T for 300/50 E2 100nm UNIMPL samples for proton (E=300MeV) and Co-60 irradiations.

Figures 15 – 17 compare ΔV_T data for 300/50 samples with those for 690/15 samples for three different proton energies. Only the data for lidded samples are shown, similar data for de-lidded samples are not reliable (see Discussion and Conclusions section for more details).

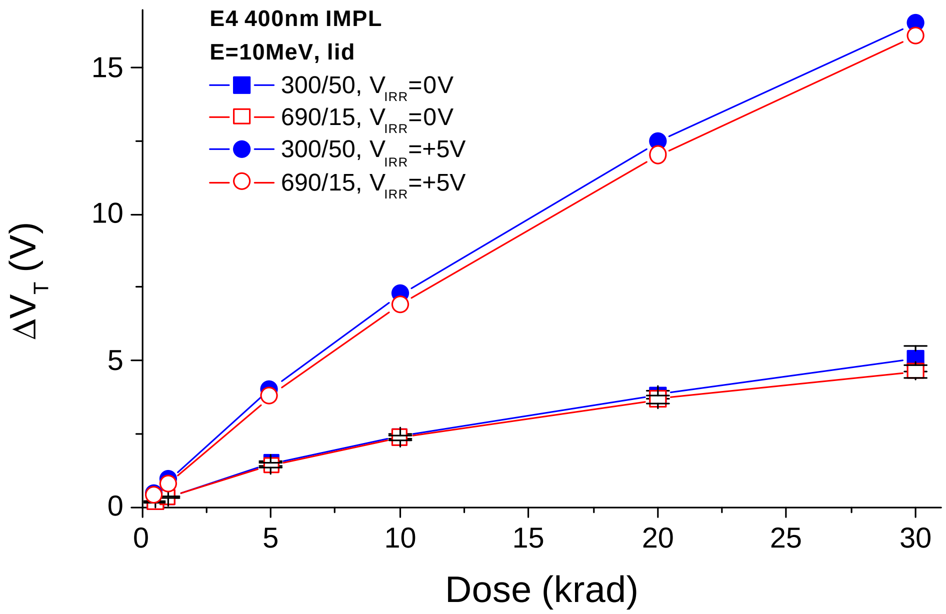

Figure 15: ΔV_T for 300/50 and 690/15 E4 400nm IMPL samples for proton irradiation (E=10MeV); lidded samples.

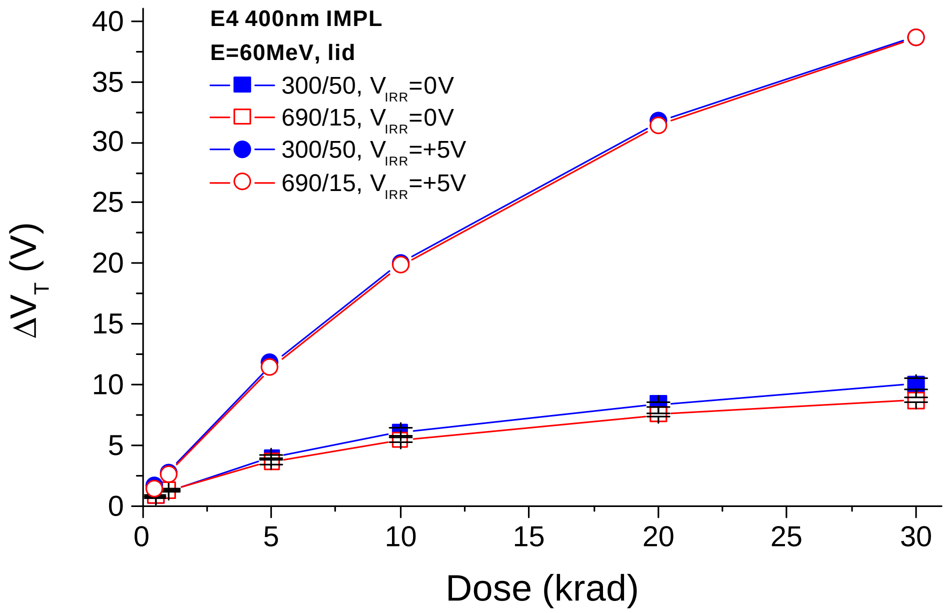

Figure 16: ΔV_T for 300/50 and 690/15 E4 400nm IMPL samples for proton irradiation (E=60MeV); lidded samples.

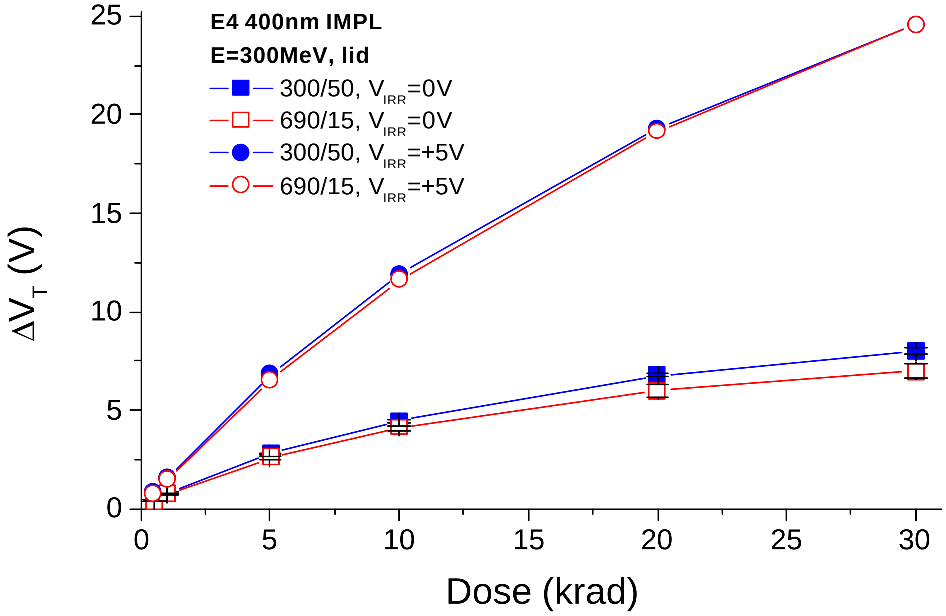

Figure 17: ΔV_T for 300/50 and 690/15 E4 400nm IMPL samples for proton irradiation (E=300MeV); lidded samples.

Figures 18 – 27 show proton energy dependencies for various 300/50 samples.

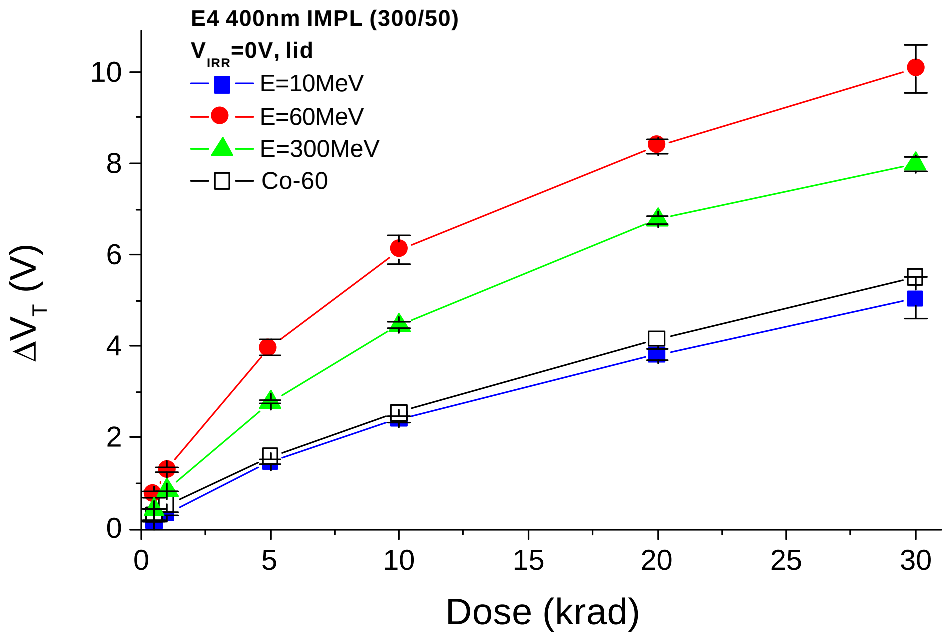

Figure 18: ΔV_T for E4 400nm IMPL 300/50 lidded samples for different proton energies; V_{IRR}=0V.

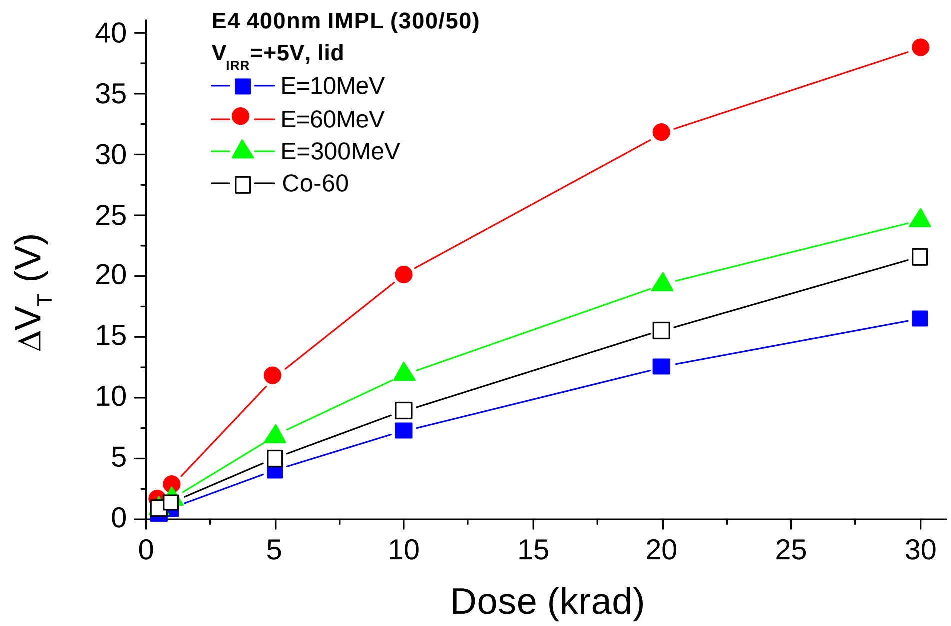

Figure 19: ΔV_T for E4 400nm IMPL 300/50 lidded samples for different proton energies; V_{IRR}=+5V.

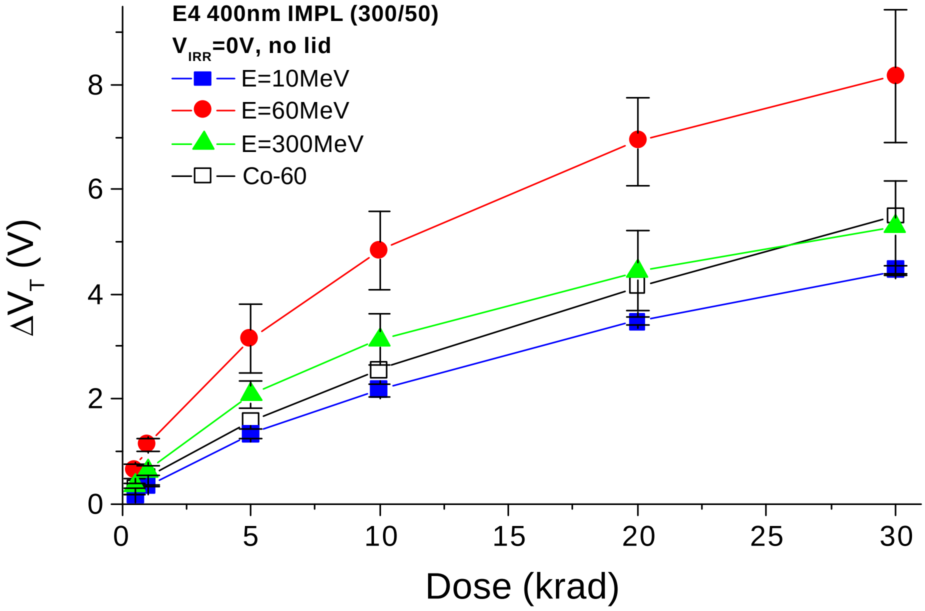

Figure 20: ΔV_T for E4 400nm IMPL 300/50 de-lidded samples for different proton energies; V_{IRR}=0V.

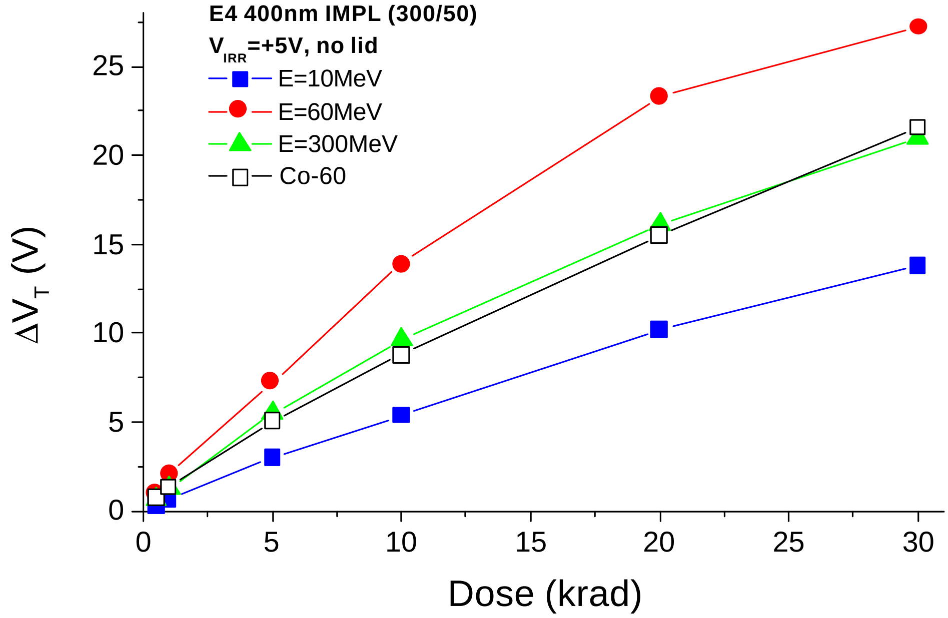

Figure 21: ΔV_T for E4 400nm IMPL 300/50 de-lidded samples for different proton energies; V_{IRR}=+5V.

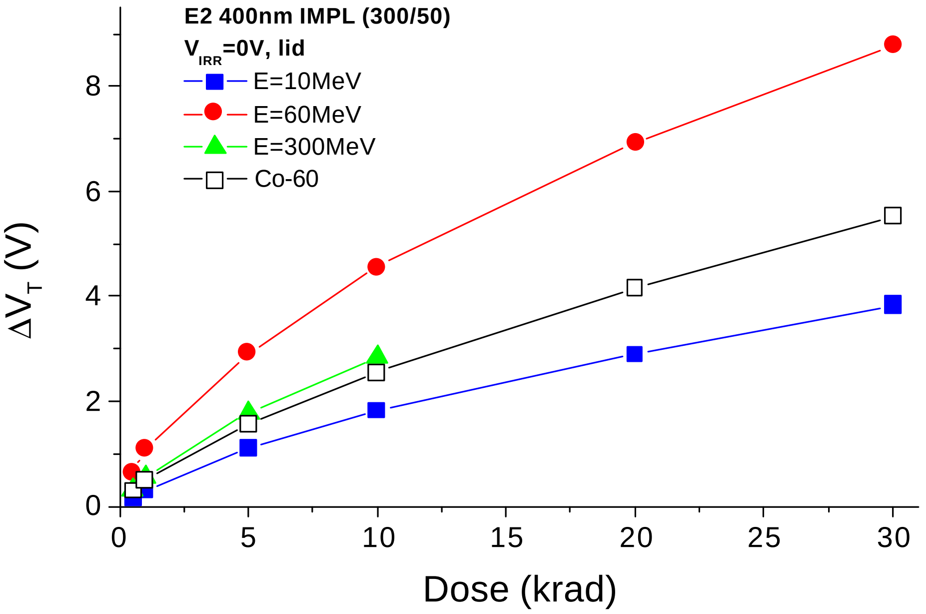

Figure 22: ΔV_T for E2 400nm IMPL 300/50 samples for different proton energies; V_{IRR}=0V.

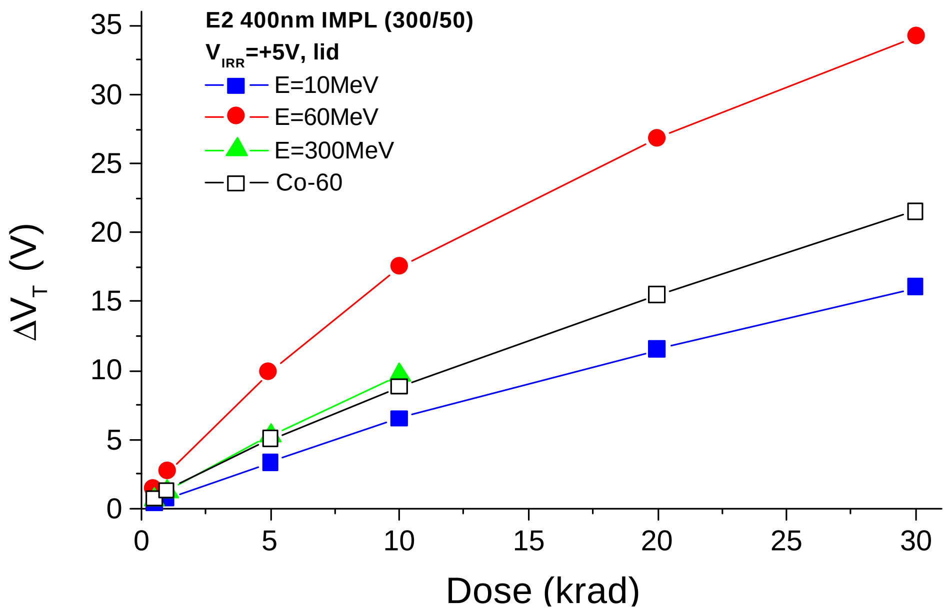

Figure 23: ΔV_T for E2 400nm IMPL 300/50 samples for different proton energies; V_{IRR}=+5V.

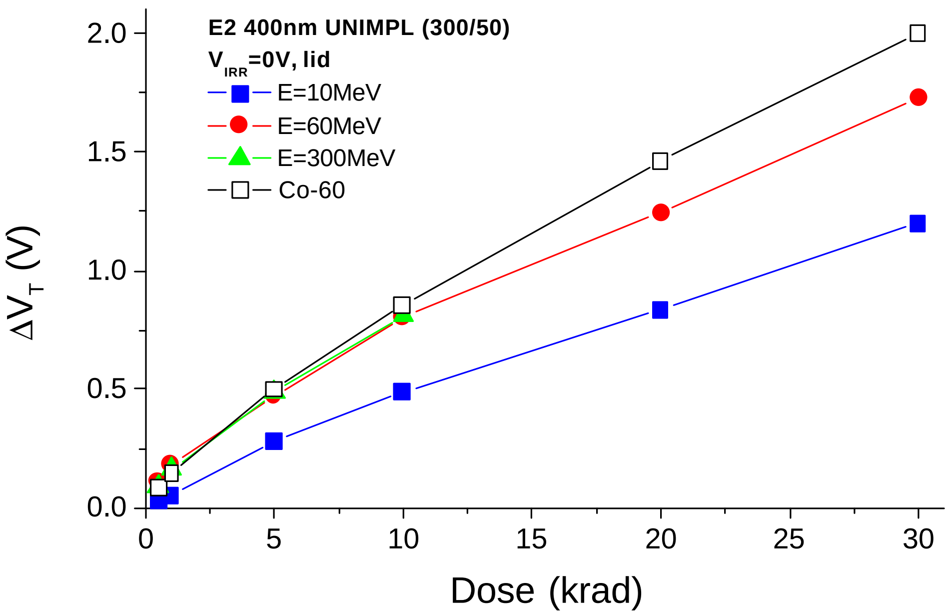

Figure 24: ΔV_T for E2 400nm UNIMPL 300/50 samples for different proton energies; V_{IRR}=0V.

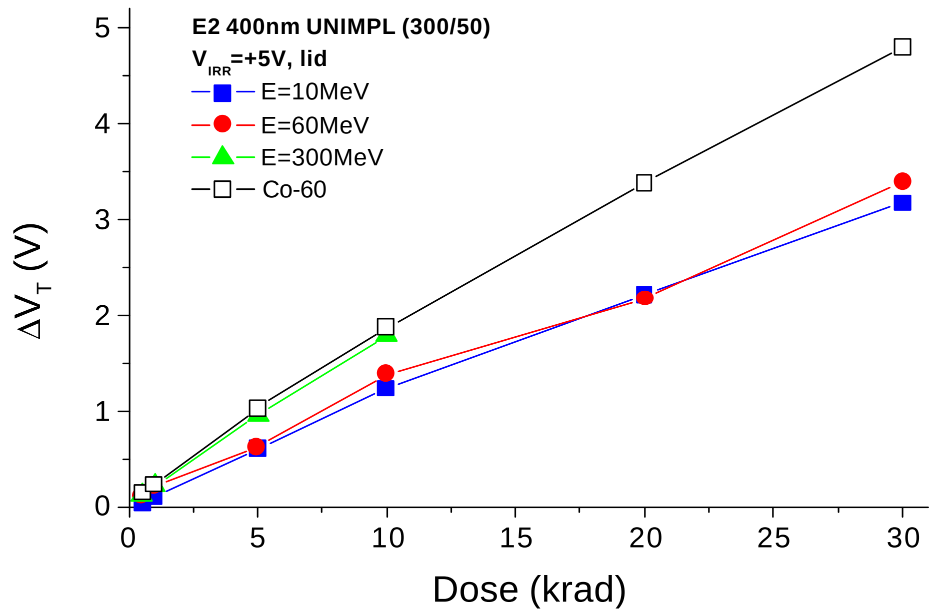

Figure 25: ΔV_T for E2 400nm UNIMPL 300/50 samples for different proton energies; V_{IRR}=+5V.

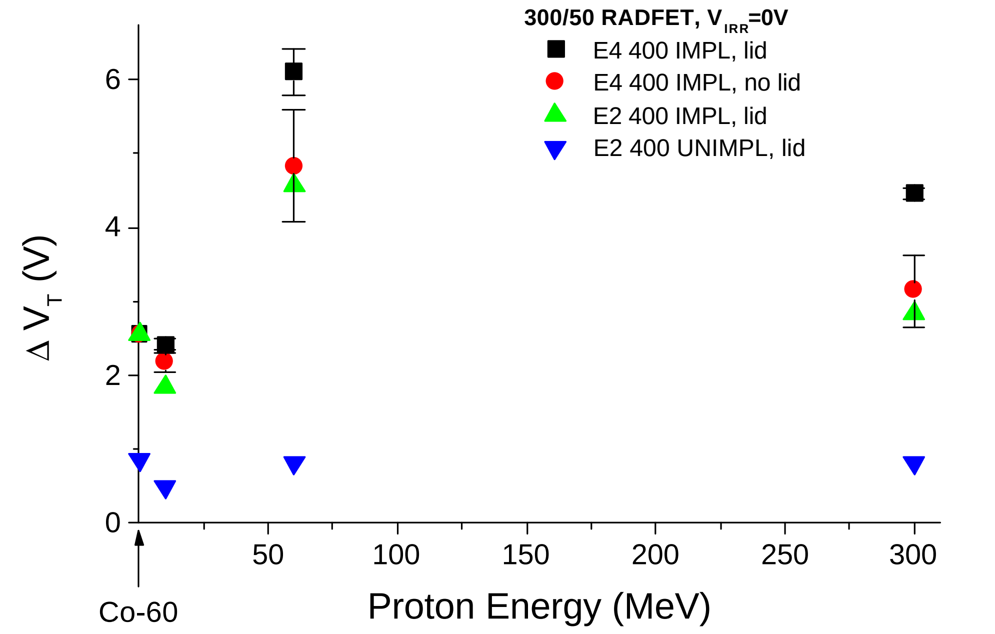

Figure 26: ΔV_T dependence on proton energy for different 400nm 300/50 samples; V_{IRR}=0V.

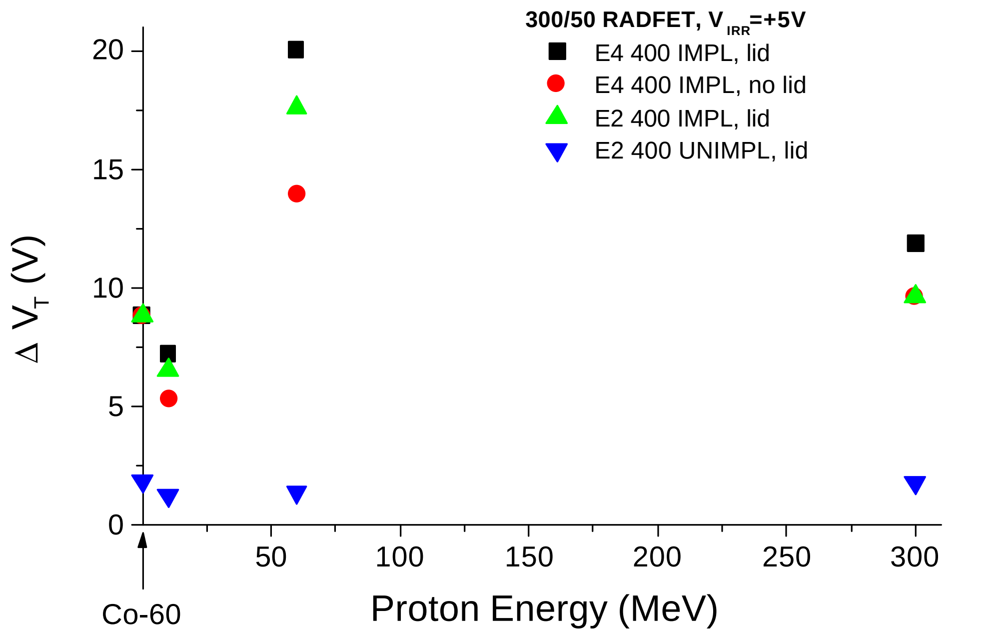

Figure 27: ΔV_T dependence on proton energy for different 400nm 300/50 samples; V_{IRR}=+5V.

Summary

Presented experimental results can be summarised as follows:

- In general, there are discrepancies between the proton data obtained and existing Co-60 data.
- In general, there is energetic dependence of RADFET proton response. The details of proton response at three energies examined are dependent on device type, mask-set revision, device geometry and package lids, as follows:
  - Device type: The discrepancies are most pronounced for 400nm IMPL devices, and much less pronounced for 400nm UNIMPL and 100nm UNIMPL RADFETs. It should be noted, however, that the results for unimplanted devices do not have statistical weight and can be regarded only as preliminary. An interesting and statistically rather established fact is that for 400nm IMPL devices Co-60 response is higher than response to 10MeV protons, significantly lower then response to 60MeV protons and somewhat lower then response to 300MeV protons.
  - Mask-set: Proton response of E4 devices is generally higher than that of E2 devices.
  - Device geometry: There is some difference between the responses of 300/50 and 690/15 E4 400nm IMPL devices. The 690/15 device exhibits somewhat lower ΔV_T (similarly to Co-60 irradiation results), and the difference from 300/50 RADFET is more pronounced for V_{IRR}=0V (not observed with Co-60).
  - Package lids: The presence of package lids acts to significantly enhance proton energy dependence.
- The irradiation bias V_{IRR} has only a quantitative effect. Namely, as in the case of Co-60 irradiation, positive V_{IRR} acts to increase ΔV_T, but the energy dependence and other relevant details of the response (e.g. effects of device type, package lids, etc.) qualitatively stay the same.
- Variations between the samples in the sample groups are bigger than in the case of Co-60 irradiation.

Discussion and Conclusions

Some of the results and discrepancies summarised above may be attributed to the experimental uncertainties. The experimental errors may come from measurement errors and proton beam non-uniformities. As the threshold voltage was measured using an established and verified method and circuitry and a high quality measurement instrument (see description of experimental details), measurement errors can most probably be regarded as negligible.

However, it seems that this is not exactly the case with beam non-uniformities. The PSI estimated a beam uniformity to be better than 5%, measured from the centre of the beam (reference point) toward the edge of the irradiated area. The irradiated area was 5 cm in diameter and could accommodate 6-8 RADFET chips. The RADFETs at the opposite sides of the irradiated area were some 4-5 cm apart, which would lead to the maximum error of some 10%. Figure 28 shows ΔV_T for the sample group No. 11 in Table 12. This sample group consists of I-074/1, I-074/3, I-072/3 and I-067/3 de-lidded samples, all irradiated with V_{IRR}=0V, and is related to the irradiation run 3.1 in Table 3. The locations of all six samples belonging to this run are given as an inset in Figure 28, centre of the beam is marked with “x”. It can be seen from ΔV_T data that there is some 25-35% difference between the RADFETs that are 5 cm apart vertically, while there is excellent agreement between the RADFETs which are close to each other (I-072/3 and I-067/3; as well as I-074/1 and I-074/3). This suggests that the reason for discrepancies may be the beam non-uniformity, in this case in vertical direction. The described problem is particularly relevant for de-lidded devices, as they were typically placed at the opposite sides of irradiated area, as on the inset of Figure 28.

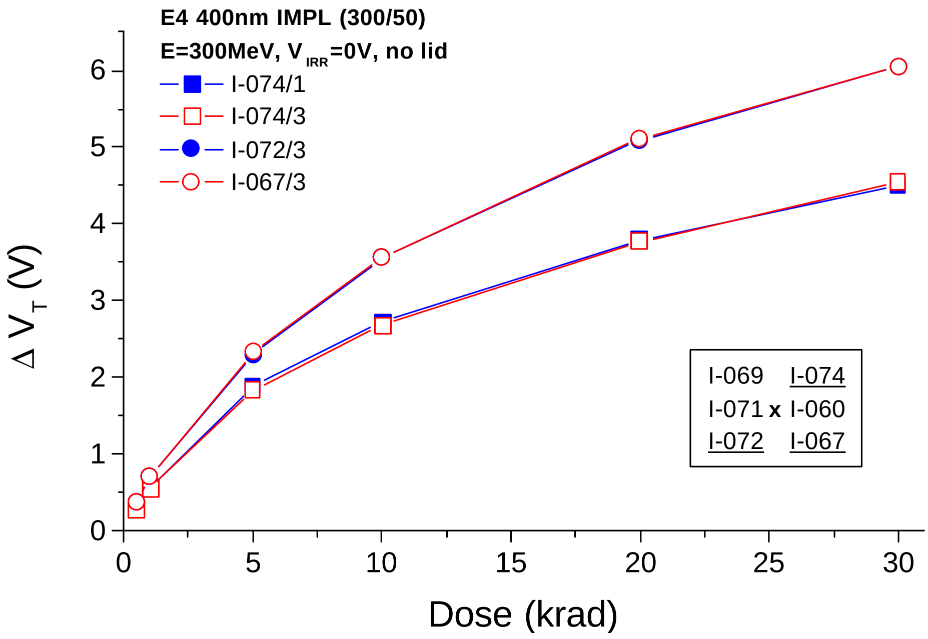

Figure 28: Illustration of possible proton beam non-uniformities as a reason for discrepancies in the experimental data. The analysed de-lidded samples belong to irradiation run 3.1 in Table 3. The locations of all six samples are given in an inset; beam centre is marked with "x", de-lidded samples are underlined.

It is plausible to assume that some of observed discrepancies (e.g. effects of mask-set and device geometry, variation between the samples) are at least partially caused by described beam non-uniformities. However, the main effects (proton energy dependence, lid effects) can not be the consequence only of experimental errors. The possible reasons for observed effects are:

- Variations in dose enhancement between Co-60 and proton exposures at different energies (this includes clearly observed effect of package lids, but also the effect of metal die attach pad on the back of the die via back-scattering).
- Increased/decreased electron-hole recombination in the gate oxide for Co-60 and protons with different energies (different contributions of columnar and geminate recombinations).
- Different energies needed per electron-hole pair creation for Co-60 and protons with different energies.
- Different contribution of non-ionising energy transfer (displacement damage) for Co-60 and protons with different energies.

The above assumptions were made on the basis of a limited literature research [4], more work is needed to elucidate which of these effects play a dominant role in NMRC RADFETs proton response. The proposed course of actions in the near future is:

- Perform an extensive literature survey related to relevant issues that have arisen from the PSI campaign.
- Perform detailed simulations of RADFET proton response using the established software packages (SHIELD, SRNA) and clarify the pertinent details of the response, as discussed above.
- Design and perform detailed experiments aimed to clarify the following aspects of proton response:
  - Package lid and die-attach pad effects (accommodate chip packages with minimum use of metal),
  - The influence of displacement damage (monitor a diode on a RADFET chip).

References

[1] Final report on MTSL dosimeter development and supply programme for 1999/2000.
[2] W. Hajdas, J. Bialkowski, U. Wyser, A. Mohammadzadeh, R. Nickson, B. O'Connell, "Sensitivity of the SREM RADFET dosimeters for STRV-1C to various proton and gamma radiation Environments", *Proceedings of RADECS'99 Conference*, Fontevraud, France, 1999. pp. 110-113.
[3] "ESAPMOS4 RADFET design layout description", document dated 20/05/1999.
[4] R.L. Pease, M. Simons, P. Marshall, "Comparison of pMOSFET total dose response for Co-60 gammas and high-energy protons", *IEEE Trans. Nucl. Sci.*, Vol. 48, No. 3, 2001; and references therein.